NUMERICAL STUDY OF MAGNETOHYDRODYNAMICS

by

TAKAHIRO SONODA

Presented to the Faculty of the Graduate School of
The University of Texas at Arlington in Partial Fulfillment
of the Requirements
for the Degree of

MASTER OF SCIENCE IN AEROSPACE ENGINEERING

THE UNIVERSITY OF TEXAS AT ARLINGTON
December 2007

ACKNOWLEDGEMENTS

During the course of study at UTA, what I have learned are many ingredients for the richness of life, love, kindness, and patience. Without families, some faculty members, and friends around me, this lesson would not have been genuine.

I would like to express great gratitude to my supervisor, Dr. Brian Dennis, who is always respecting my research interest and providing great lectures in finite element methods, numerical methods in general, and practical programming techniques.

I am also grateful to Dr. Zhen Xue Han who is willing to spend time with me for the discussion of finite volume solver. His knowledge and experience in this field has triggered my motivation to learn and practice more in CFD.

I thank Dr. Lu who kindly let me work at aerodynamics research center while I was in undergraduate school at UTA. Without him, I would not have been able to develop such a great deal of interest to experimental aerodynamics and propulsions. A collection of flow visualization photos that I took with his tremendous amount of help will be a treasure in the future.

I must express thanks to Dr. Dale. A. Anderson who helped me to see excitement and peculiarity in learning. He was the reason why I came to a decision to pursue Master's degree in computational fluid dynamics.

I owe my friends in CFD lab great deal of kindness. Time we shared in our lab by discussing problems is an asset in my college life. My friends from different cultural

backgrounds have shaped my identity for last six years in many ways. It has been a great pleasure to live and learn in this diverse community.

It is my kind and loving parents who gave me a ticket to go outside of the country to learn more about the world. I cannot describe how thankful I am to my parents and the brother in Japan. Their enduring love has helped me to focus on accomplishing my academic goals in the United States.

November 21, 2007

ABSTRACT

NUMERICAL STUDY OF MAGNETOHYDRODYNAMICS

Publication No. ______

Takahiro Sonoda, AE

The University of Texas at Arlington, 2007

Supervising Professor: Brian H. Dennis

Use of electromagnetic fields has been shown to be an effective way to control the behavior of electrically conducting fluids. Specifically, the modification of the boundary layer profile with electromagnetic fields can yield performance improvements such as reduced drag and improved heat transfer. Though this approach has been demonstrated computationally and experimentally with conducting liquids (i.e. seawater), application to aerodynamic devices operating in air has not seen the same success.

Through the use of numerical simulation and eventually optimization, we hope to develop efficient designs that are effective for boundary layer control for low temperature conducting gases (non-thermal plasmas). The boundary layer control technique requires an electrically conducting fluid within the boundary layer and either intense magnetic fields or high voltage difference across electrode pairs. The plasma discharge at atmospheric pressure was suggested to ionize air and thus increase the electrical conductivity of the air.

A numerical model was developed to assist in the design of physical experiments and to enhance the understanding of the physical mechanism of the plasma flow under the influence of electromagnetic fields.

The model equations governing the flow of non-thermal plasmas in an electromagnetic field were discretized using finite volume method for MHD fluid equations and Galerkin finite element method for MHD electrodynamics equations on an unstructured mesh.

It was observed that flows at low Reynolds number can be altered by electromagnetic fields with low applied voltage and relatively low magnetic flux density under the assumption of constant electrical conductivity of plasma.

TABLE OF CONTENTS

Appendix

LIST OF ILLUSTRATIONS

LIST OF TABLE

Table Page

CHAPTER 1

INTRODUCTION

The possible use of magnetohydrodynamics (MHD) to aerospace engineering applications has been revisited by research communities in recent years. This trend might owe to some of the technological improvements in magnetic materials and power source devices in the last few decades. Along with the availability of the more advanced technology, demands for better performance in engineering applications are always soaring. MHD applications are conceptually attractive although the power input required to obtain appreciable effects in the gas medium may be economically prohibitive at this time.

Feasibility study of MHD techniques plays an important role in the design and development of MHD devices. The desired MHD effects must be obtained by supplying reasonable amount of power input and having a magnetic device with attainable magnetic field strength.

1.1 Concept of MHD actuator

The fundamental concept of the MHD techniques is that charges moving through an electromagnetic field experience a Lorentz force and an increase in energy. This microscopic behavior of particle kinetics results in the macroscopic behavior of the flow. In addition to Lorentz force, electric fields are capable of doing work on charged particles, which results in the change in energy of the flow without any mechanical contact, called Joule heating. These two effects make a significant difference between behaviors of the electrically conducting and non-conducting flow. The fundamental of MHD actuator is to determine the way to apply electric and magnetic fields so that the flow can be altered as desired.

1.2 Types of MHD devices

Either flow acceleration through power input or electricity generation through extraction of power from the flow are the common operating principles among all the MHD devices. Potential use of MHD technique for aerospace applications can be further categorized into several disciplines according to its purpose as an engineering devise.

1.2.1 MHD accelerated flow wind tunnel

There is a limit to which Mach number of the flow at test section in hypersonic facility can be increased since availability of the energy depends on the total enthalpy of the flow. Conventionally, the working fluid upstream needs to be either compressed to extremely high pressure, heated to extremely high temperature, or combination of both in order to attain the extended range of test section Mach number. In addition to them, the MHD technique provides the third means to realize the above [1].

1.2.2 MHD propulsion devices

MHD propulsion devices, such as electrical propulsion systems, have been proposed for use in space flight [2, 3]. It can overcome the limitations of specific impulse that be attained by chemical rockets due to the limited availability of the total enthalpy in chemical reactions. The exhaust velocity of an engine is an essential factor to determine achievable thrust [3]. The higher exhaust velocity can be achieved by externally supplying power in the presence of magnetic field. However, as a drawback, thrust to weight ratio of MHD propulsion device is less than unity. For this reason, use of MHD propulsion devices is limited to outer space [4].

1.2.3 MHD active flow control

Passive and active flow control schemes have been extensively studied since 1918 [4]. At the early stage of study, it was found that the boundary layer plays an important role in the flow control. The primary objective of flow control methods is to reduce the large energy losses in the flow. As a means of energizing the flow to overcome an adverse pressure gradient in the boundary layer regions, MHD flow acceleration may prevent the boundary layer from separating [2].

1.2.4 MHD power generation

The MHD electric power generator is based upon the Faraday effect; that is, a conductor which moves through a magnetic field generates within it an induced electric current. The MHD generator uses ionized gases that are produced through heating by chemical or nuclear fuel as the moving conductors [2]. Thermal ionization of gases that is crucial to this application takes place only at extremely high temperatures.

1.3 Review of MHD research

Though the subject of MHD has been understood since the fundamental experiments of Hartmann and Lazrus in the 1930’s, aerospace applications using plasma have not been fully developed. This is due to the low electrical conductivity of atmospheric gases and the significant power input required to cause substantial alternation in flow [2].

Recently, interest in MHD techniques for use with non-thermal plasmas has been found with the aerodynamics community. However, the main barrier to the practical usage of MHD for aerodynamics is the low electrical conductivity of the working gas. In order to increase the electrical conductivity of the gas, the use of discharge plasma under the atmospheric condition was found to be effective. The weakly ionized gas is generated by secondary electronic emission from embedded electrodes on control surfaces. The generated plasma consists of electrons in a highly excited state, however the heavy ions retain the thermodynamic condition of its surrounding neutral particles.

Some of the experimental and numerical attempts for analysis of MHD in non-thermal plasma conditions are reviewed in the following sections.

1.3.1 Experimental study

Quite a few experimental works have been conducted in electrohydrodynamics (EHD), where the air is weakly ionized by di-electric discharge plasma and energized due to the deposition of energy in the form of, joule heating [5]. Significant shifts in the aerodynamic forces over a broad range of angles of attack were reported using plasma actuators [8, 9]. This technique was further applied to the separation control of low-pressure turbine blades [10]. Plasma actuator was arranged in such a way that a steady two-dimensional wall jet effect is induced downstream of the actuators. It was reported that comparable effect to vortex generators was measured.

Use of a magnetic field in addition to the plasma discharge has been considered to provide more significant alternation of flow. Experimental work on flow control with MHD for aerospace applications mainly focuses on drag reduction and increase in lift. However, the mechanism of alternation of the flow is still uncertain [6]. Further investigations need to be done in order to obtain desired alternation of the flow.

MHD flow control for the application where thermal plasma is not present, can be realized by having plasma discharge and magnetic field applied in the plasma flow [6]. In this experiment, a hypersonic flow was altered by using discharge plasma and applying magnetic field. The range of magnetic flux density applied perpendicular to the plasma current flow direction and the air flow, is between -0.2 and 0.2 Tesla. Furthermore, the mean applied voltage ranges from 600 to 1600 volts. The results show that the change in lift and drag is on the order of a few grams in hypersonic flow [6].

An important parameter in MHD is a value of electrical conductivity for the fluid medium. It directly corresponds to the degree of ionization of the gas and the strength of the applied electromagnetic field. Recent efforts have been made to measure the electrical conductivity of supersonic nonequilibrium plasma [7]. The measured conductivity under the magnetic field of 1.0 Tesla ranges from 0.02 to 0.06 [mho/m].

1.3.2 Numerical study

In order to model the flow physics of electrically conducting medium, MHD equations are utilized. The equations are derived by taking the moments of Boltzman equations developed in the kinetic theory [2]. The Boltzmann equations have three independent variables in physical space, another set of three independent variables in velocity space, and time. In addition to the flow equations, Maxwell's equations are also required to model the electromagnetic properties. Thus, these two sets of governing equations are the so-called MHD equations, and are commonly used in astrophysics.

Rigorous derivations of MHD equations are available in the literatures [2]. Most of existing mathematical models of MHD flow in aerospace applications exploit the standard MHD equations with augmented equations with additional components.

MHD simulations in the past for aerospace applications have been developed in a context of thermal plasmas. In other words, the air enters a dissociated state due to the addition of heat. In thermal plasma, the chemical reactions take place due to the significant amount of energy deposition into the gas. High temperature flow physics have been studied extensively during the development of re-entry vehicles such as Apollo and the Space Shuttle in order to predict the durability of heat shielding materials.

A typical approach to model the thermal plasma is to consider the chemical reactions and flow equations [11]. Furthermore, more detailed simulations have considered the two-temperature model by noting that the temperature of the heavy particles and electrons differs [12, 13]. Theoretically, each species can have its own temperature. However, this model approximates the temperature of heavy particles as one temperature since the mass of heavy species are somewhat similar. On the other hand, the mass of an electron is insignificant compared with other species. According to the definition of the temperature, the temperature of electrons deviates from the other heavy species.

In the high temperature weakly ionized gas, transport properties and the electrical conductivity can be computed using the collision cross sections [2] estimated from the binary collision model [14, 15, 16]. The electrical conductivity can be also derived from the kinetic theory with the experimentally obtained collision cross section [2].

One of main difficulties in modeling of MHD at the low temperature is based on the fact that the working medium such as air needs to be ionized using a secondary ionization source in order to increase the electrical conductivity. This can be done through electron beams [17] and glow discharge or dielectric barrier discharge. Thus, this raises the necessity to derive the mathematical model of the plasma discharge across the electrodes, which involves the knowledge of detailed collision models [18, 19].

The role of the electron temperature that represents the kinetic energy of the electrons becomes more significant in non-thermal plasma. The plasma reaction in non-thermal condition can be initiated only by the collisions of secondary electrons emitted from the electrodes to other air molecules. Electron collisions may excite the molecules to the meta-stable state, which now is an active species. Though meta-stable atoms and molecules exist for only a short period of time, they play an important role in non-thermal plasma chemistry [18]. A considerable number of species needs to be taken into account if the detailed plasma chemistry is to be modeled completely and that, results in large number of unknowns. Furthermore, chemical kinetics of most of reactions has not been measured or cannot be measured [18]. More fundamental research in cold plasma chemistry needs to be conducted before one can form a complete mathematical model to simulate these complex reactions.

Slight variations in the modeling of non-thermal MHD flow can be observed among the literature. This is due to the difference in modeling of plasma discharge.

A primitive model of discharge plasma called a phenomenological model of discharge plasma was used to model MHD hypersonic flow control [22]. This model consists of MHD equations, the charge conservation equation, and the generalized Ohm’s law. The explicit model of the electrical conductivity was derived simply based on the observation of the phenomenon. The electrical conductivity decreases as the distance from the electrodes increases.

In a slightly more sophisticated mathematical model, discharge plasma is modeled by a drift-diffusion glow discharge model [23]. In this model, the charge conservation equation, the generalized Ohm’s law, and the external circuit equation are exploited. In addition to those, the electric field was updated according to the change in the distribution of charge density. As a variation of this model, it was suggested to replace generalized Ohm’s law with the momentum equations for the charged species [24]. Since the generalized Ohm’s law was derived from the electron-momentum equation, the ion-momentum equation, and the overall momentum equation [2], this approach seems to be reasonable. Under an assumption of the low magnetic Reynolds number, the induced magnetic field was not computed.

In chapter_2, the governing equations for MHD are discussed. Maxwell’s equations will be discussed in detail in order to see the consistency of the equations.

In chapter_3, the numerical methods used to solve the MHD equations will be discussed.

In chapter_4, a finite volume flow solver developed at the UTA CFD Lab was validated for Poisuille flow and the internal flow around the turbine blade.

In chapter_5, simulation results for the use of MHD technique to modify the flow field are presented.

CHAPTER 2

GOVERNING EQUATIONS

2.1 Derivations of MHD equations

MHD equations consist of two sets of equations, fluid equations and electromagnetic equations. The fluid equations describe the flow physics under the influence of the electromagnetic fields. They have a form of the Navier Stokes equation in classical fluid dynamics with additional terms due to the effect of EMF, namely, Lorentz force and Joule heating. The electromagnetic equations describe the electromagnetic field due to both externally applied and induced fields. Full description of the behavior of electromagnetic fields is realized by Maxwell's equations. In this work, the Maxwell's equation will be simplified using appropriate approximations.

2.1.1 Velocity distribution function

In microscopic level, the molecules of fluid collide with each other and the collisions transmit the change in the state of the bulk flow. In addition to the large number of collisions, the particles have a distribution of speeds; that is, they are not isoenergetic. The collisions between particles not only change the direction of motion, but in addition, one particle can transfer part or all of its kinetic energy to another particle [2].

One treats those particles which at a given time have velocities in some small range of velocity. In order to do that, the velocity distribution function is introduced.

The velocity distribution functions represent the probability of the number of particles with a certain velocity range at a certain point.

2.1.2 Moments of Boltzmann equations

Since the exact distribution function cannot be obtained, the problem must be simplified by considering only gross properties, such as density, velocity, and thermal energy. Furthermore, when there exist a large number of collisions such as in weakly ionized plasma, the perturbing effect of external fields on the particle motion is small. Thus, the average perturbing effect on a large number of particles is analyzed.

By integrating the Boltzmann equation, whose solution is the distribution function with respect to a certain velocity ranges, the conservation equations can be obtained. It should be noted that conservation equations can be derived only for those quantities which are conserved by the particles during collision; mass, charge, momentum, and energy. These are the first half of MHD equations that describe the flow physics under the influence of the electromagnetic fields.

2.2 Fluid equations

The first half of MHD equations is a set of fluid equations. They are consisted of the first three moments of the Boltzmann equation, conservation of mass, momentum, and energy.

It should be noted that fluid equations have the same mathematical expression as the Navier Stokes equations in the ordinary fluid dynamics except the source terms on the right hand side, body force in each component of momentum equations and the

Joule heating in the energy equation. MHD fluid equations in a differential form are written in Cartesian coordinates as following.

$$\frac{\partial \tilde{\rho}}{\partial \tilde{t}} + \frac{\partial}{\partial \tilde{x}}\left(\tilde{\rho}\tilde{u}\right) + \frac{\partial}{\partial \tilde{y}}\left(\tilde{\rho}\tilde{v}\right) = 0 \tag{2.1}$$

$$\frac{\partial\left(\tilde{\rho}\tilde{u}\right)}{\partial \tilde{t}} + \frac{\partial}{\partial \tilde{x}}\left(\tilde{\rho}\tilde{u}^2 + \tilde{p} - \tilde{\tau}_{xx}\right) + \frac{\partial}{\partial \tilde{y}}\left(\tilde{\rho}\tilde{u}\tilde{v} - \tilde{\tau}_{yx}\right) = \tilde{J}_y\tilde{B}_z \tag{2.2}$$

$$\frac{\partial\left(\tilde{\rho}\tilde{v}\right)}{\partial \tilde{t}} + \frac{\partial}{\partial \tilde{x}}\left(\tilde{\rho}\tilde{v}\tilde{u} - \tilde{\tau}_{xy}\right) + \frac{\partial}{\partial \tilde{y}}\left(\tilde{\rho}\tilde{v}^2 + \tilde{p} - \tilde{\tau}_{yy}\right) = -\tilde{J}_x\tilde{B}_z \tag{2.3}$$

$$\begin{aligned} &\frac{\partial \overline{E}_t}{\partial t} + \frac{\partial}{\partial x}\left[\overline{E}_t u + \left(-K_t\frac{\partial T}{\partial x}\right) + pu - u\tau_{xx} - v\tau_{xy}\right] \\ &+ \frac{\partial}{\partial y}\left[\overline{E}_t v + \left(-K_t\frac{\partial T}{\partial y}\right) + pv - u\tau_{yx} - v\tau_{yy}\right] = J_xE_x + J_yE_y \end{aligned} \tag{2.4}$$

The right hand side, the source terms, of the governing equations should be discussed in details since they differ from Navier-Stokes equations. In 2-D model, only two terms from the cross product of the total current density and the magnetic field appear. It is a limitation of the 2-D model that only a certain directions of current and the magnetic field can be retained. As shown in equations, the directions of the current can be in any directions in the computational domain. Only z-component, normal to the gage, of the magnetic field is considered in this model. The source terms in the energy equation represents the Joule heating, addition of the energy from the electric field to the flow.

It should be noted that the current density that appears in the conservation of momentum and the energy equations is the total current density. Thus, the definition of the electric current should be clearly noted [2].

$$\vec{J} = \sum_s \vec{J}_s = \sum_s n_s e Z_s \vec{V}_s + \vec{v}\sum_s n_s e Z_s = \vec{j} + \vec{v}\rho_e \tag{2.5}$$

If the gas is electrically neutral, the convection current vanishes. Thus, the total current is the same as the conduction current.

$$\rho_e = \sum_s n_s e Z_s = 0 \tag{2.6}$$

With Eqn2.6, total current density is equivalent to conduction current density. In order to calculate the conduction current density, generalized Ohm's law was used. Generalized Ohm's law is derived from the electron-momentum equation, the ion-momentum equation, and the overall momentum equation [2]. It implicitly relates the conduction current density with the total electric and magnetic fields. The final version of Ohm's law in a partially ionized gas can be written as

$$\vec{j} = \sigma\left(\vec{E} + \vec{v} \times \vec{B}\right) - w_e \tau_e{}^* \vec{j} \times \frac{\vec{B}}{B} + f^2 w_e \tau_e{}^* w_I \tau_{In}{}^* \left[\frac{\vec{B}}{B}\left(\frac{\vec{B}}{B} \cdot \vec{j}\right) - \vec{j}\right] \tag{2.7}$$

The ion-slip, the last term and the hall current, the second term, are also not considered in the simulation, which leads to a simpler expression of Eqn2.7. Now, the total current density can be explicitly written in terms of electrical conductivity, electric field, average flow velocity, and magnetic flux density.

$$\vec{J} = \vec{j} = \sigma\left(\vec{E} + \vec{v} \times \vec{B}\right) \tag{2.8}$$

2.3 Maxwell's equations

The second half of MHD equations is a set of simplified Maxwell's equations. As discussed in 2.1, Electromagnetic field needs to be prescribed to compute the Lorentz force and the Joule heating in the flow equations.

2.3.1 Total current density and induced magnetic field

The relation between the magnetic flux density and the total current density is obtained from the Ampere's law. Two simplifications will be made with this relationship.

$$\mu_0\left(\vec{J} + K_0\frac{\partial \vec{E}}{\partial t} + \nabla \times \vec{M}_p\right) = \nabla \times \vec{B} \tag{2.9}$$

The first simplification can be made using the analysis of the order of magnitude. The second term, displacement current that represents the change in electric field induces the magnetic field can be neglected in engineering applications by comparing the first two terms. Furthermore, the magnetization current was neglected.

$$\mu_0\vec{J} = \nabla \times \vec{B} \tag{2.10}$$

The second simplification can be made when this relationship is non-dimensionalized. For the low Reynolds magnetic number, the induced magnetic field due to the current can be neglected, which is $\left\|\vec{b}\right\| << \left\|\vec{B}_0\right\|$. For most of aerospace applications, the magnetic Reynolds number is small. Thus, only insignificant induced magnetic field is produced and neglected. As a result, this relationship is not required since the total current density can be computed using Ohm's law and only the externally applied magnetic field is considered.

2.3.2 Conservation of magnetic flux density

As discussed in the previous section, the induced magnetic field due to the total current is neglected in this simulation. Thus, the only externally applied magnetic field is considered. This magnetic field needs to satisfy the following mathematical relationship that Maxwell's equation presents.

$$\nabla \cdot \vec{B} = 0 \tag{2.11}$$

2.3.3 Faraday's law

Since the induced magnetic field due to the total current is neglected and the externally applied magnetic field is time invariant, electric field decouples with magnetic field.

$$\nabla \times \vec{E}' = -\frac{\partial \vec{B}}{\partial t} = 0 \tag{2.12}$$

Thus, the electrical potential that satisfies the above equation can be introduced. Introducing the potential is computationally advantageous since the number of unknowns can be reduced in our governing equations.

$$\vec{E} = -\nabla \phi \tag{2.13}$$

In the time-dependent or quasi-stationary case, the electrostatic and magnetostatic fields are completely uncoupled. This is no longer true in time-dependent problems. The electric field that appears in this equation is the induced electric field due to the time rate of change in magnetic flux.

$$\nabla \times \vec{E}' = -\frac{\partial \vec{B}}{\partial t} \tag{2.14}$$

$$\vec{B} = \nabla \times \vec{A} \tag{2.15}$$

$$-\frac{\partial \left(\nabla \times \vec{A}\right)}{\partial t} = \nabla \times \vec{E}' \tag{2.16}$$

$$-\nabla \times \frac{\partial \vec{A}}{\partial t} = \nabla \times \vec{E}' \tag{2.17}$$

$$\vec{E}' = -\frac{\partial \vec{A}}{\partial t} \tag{2.18}$$

In addition to the induced electric field, there may also be present an electrostatic field such as the externally applied static field, $\vec{E}'' = -\nabla\phi$. Accordingly, the total electric field can be defined as

$$\vec{E} = \vec{E}' + \vec{E}'' \tag{2.19}$$

$$\vec{E} = -\frac{\partial \vec{A}}{\partial t} - \nabla\phi \tag{2.20}$$

$$\vec{E} = -\nabla\phi \tag{2.21}$$

Therefore, as long as the electric potential is introduced as the described relation above, Faraday's law can be satisfied.

2.3.4 Gauss's law

The last equation of Maxwell's is the Gauss's law. Gauss's law represents that the presence of the charge density produces the electric field in the domain.

$$K_0 \nabla \cdot \vec{E} = \rho_e \tag{2.22}$$

In the previous section, the electric potential has been introduced. Substitution of Eqn 2.21 into the Gauss's law Eqn 2.22 results in the following relation. This is a classical PDE problem, Poisson's equation.

$$-K_0 \nabla^2 \phi = \rho_e \tag{2.23}$$

It should be noted that the Maxwell's equations do not give charge density as its solution for this case. Thus, the excess charge density needs to be computed using another physical relationship. An equation that describes the dynamics of the charges is the conservation equation of charges.

However, in this work, the neutrality of the medium is assumed. In other words, the excess charges are not present in the medium. Thus, the Gauss's law can be simplified and results into Laplace's equation.

$$-K_0\nabla^2\phi = 0 \tag{2.24}$$

$$-\nabla^2\phi = 0 \tag{2.25}$$

2.3.5 Conservation of charges

The charge conservation equation for the excess charge can be derived from the Bolzmann equation as other conservation equations. The summation of charge conservation equation for each species should be taken, which results in the overall charge conservation equation.

$$\frac{\partial \rho_e}{\partial t} + \nabla \cdot J = 0 \tag{2.26}$$

2.4 Nondimensionalized MHD equations

MHD equations are non-dimensionalized to identify the important nondimensional parameters. Reference variables used to non-dimensionalize the equations are listed below. The details derivations of the following equations are provided in Appendix A. For the total current density in the fluid equations, Ohm's law was used.

$$\frac{\partial \rho}{\partial t} + \frac{\partial}{\partial x}(\rho u) + \frac{\partial}{\partial y}(\rho v) = 0 \tag{2.27}$$

$$\frac{\partial(\rho u)}{\partial t} + \frac{\partial}{\partial x}\left(\rho u^2 + p - \tau_{xx}\right) + \frac{\partial}{\partial y}\left(\rho uv - \tau_{yx}\right) = J_y B_z \tag{2.28}$$

$$\frac{\partial(\rho v)}{\partial t} + \frac{\partial}{\partial x}\left(\rho vu - \tau_{xy}\right) + \frac{\partial}{\partial y}\left(\rho v^2 + p - \tau_{yy}\right) = -J_x B_z \tag{2.29}$$

$$\begin{aligned}&\frac{\partial \overline{E}_t}{\partial t}+\frac{\partial}{\partial x}\left[\overline{E}_t u+q_x+pu-u\tau_{xx}-v\tau_{xy}\right]\\&+\frac{\partial}{\partial y}\left[\overline{E}_t v+q_y+pv-u\tau_{yx}-v\tau_{yy}\right]=K\left(J_xE_x+J_yE_y\right)\end{aligned}\tag{2.30}$$

$$\tau_{xx}=\frac{2}{3}\frac{\eta}{\mathrm{Re}_L}\left(2\frac{\partial u}{\partial x}-\frac{\partial v}{\partial y}\right)\quad \tau_{xy}=\frac{\eta}{\mathrm{Re}_L}\left(\frac{\partial u}{\partial y}+\frac{\partial v}{\partial x}\right)=\tau_{yx}$$

$$\tau_{yy}=\frac{2}{3}\frac{\eta}{\mathrm{Re}_L}\left(2\frac{\partial v}{\partial y}-\frac{\partial u}{\partial x}\right)$$

$$q_x=-\left(\frac{\tilde{\eta}}{(\gamma-1)\mathrm{Re}_L\,\mathrm{Pr}}\right)\frac{\partial T}{\partial x}\quad q_y=-\left(\frac{\tilde{\eta}}{(\gamma-1)\mathrm{Re}_L\,\mathrm{Pr}}\right)\frac{\partial T}{\partial y}$$

The non-dimensional total current density can be written in terms of the non-dimensional electric field, magnetic flux, and Hartmann number, Reynolds, and another parameter, K.

$$\vec{J}=\begin{Bmatrix}J_x\\J_y\end{Bmatrix}=\begin{Bmatrix}\left(\frac{H_a{}^2K}{\mathrm{Re}}\right)E_x+\left(\frac{H_a{}^2}{\mathrm{Re}}\right)vB_z\\\left(\frac{H_a{}^2K}{\mathrm{Re}}\right)E_y+\left(\frac{H_a{}^2}{\mathrm{Re}}\right)(-uB_z)\end{Bmatrix}\tag{2.31}$$

$$H_a{}^2=\frac{\tilde{L}_0{}^2\tilde{B}_0{}^2\tilde{\sigma}_0}{\tilde{\eta}_0}\tag{2.32}$$

$$\mathrm{Re}=\frac{\tilde{\rho}_0\tilde{a}_0\tilde{L}_0}{\tilde{\eta}_0}\tag{2.33}$$

$$K=\frac{\tilde{E}_0}{\tilde{B}_0\tilde{a}_0}\tag{2.34}$$

2.5 Vector form of MHD equations

For the development of the algorithms, a vector form of the governing equations is used. The solution vector contains the conservative variables. The flux vector in x and y direction can be split into the inviscid flux and viscous flux.

$$\frac{\partial \vec{\mathrm{Q}}}{\partial \mathrm{t}}+\frac{\partial \vec{\mathrm{E}}}{\partial \mathrm{x}}+\frac{\partial \vec{\mathrm{F}}}{\partial \mathrm{y}}=\vec{\mathrm{S}}\tag{2.35}$$

$$\vec{\mathrm{Q}} = \begin{bmatrix} \rho \\ \rho u \\ \rho v \\ \overline{E}_t \end{bmatrix}$$

$$\vec{\mathrm{E}} = \vec{\mathrm{E}}_\mathrm{i} + \vec{\mathrm{E}}_\mathrm{v} = \begin{bmatrix} \rho u \\ \rho u^2 + p \\ \rho v u \\ \left(\overline{E}_t + p\right)u \end{bmatrix} - \begin{bmatrix} 0 \\ \tau_{xx} \\ \tau_{xy} \\ u\tau_{xx} + v\tau_{xy} + q_x \end{bmatrix}$$

$$\vec{\mathrm{F}} = \vec{\mathrm{F}}_\mathrm{i} + \vec{\mathrm{F}}_\mathrm{v} = \begin{bmatrix} \rho v \\ \rho u v \\ \rho v^2 + p \\ \left(\overline{E}_t + p\right)v \end{bmatrix} - \begin{bmatrix} 0 \\ \tau_{yx} \\ \tau_{yy} \\ u\tau_{yx} + v\tau_{yy} + q_y \end{bmatrix} \tag{2.36}$$

$$\vec{\mathrm{S}} = \begin{bmatrix} 0 \\ J_y B_z \\ -J_x B_z \\ K\left(J_x E_x + J_y E_y\right) \end{bmatrix}$$

$$\tau_{xx} = \frac{2}{3}\frac{\eta}{\mathrm{Re}_L}\left(2\frac{\partial u}{\partial x} - \frac{\partial v}{\partial y}\right) \quad \tau_{xy} = \frac{\eta}{\mathrm{Re}_L}\left(\frac{\partial u}{\partial y} + \frac{\partial v}{\partial x}\right) = \tau_{yx}$$
$$\tau_{yy} = \frac{2}{3}\frac{\eta}{\mathrm{Re}_L}\left(2\frac{\partial v}{\partial y} - \frac{\partial u}{\partial x}\right) \tag{2.37}$$

Thermal equation of state

$$p = \frac{\rho T}{\gamma} \tag{2.38}$$

Caloric equation of state

$$E_t = e + \rho\frac{u^2 + v^2}{2}\vec{V}^2 \tag{2.39}$$

The total energy can be expressed in the quantity per unit volume.

$$\overline{E}_t = e + \frac{1}{2}\rho\vec{V}^2 \tag{2.40}$$

2.6 Electrical conductivity and Magnetic dipole

Electrical conductivity is required to compute the conduction current from generalized Ohm's law. The great challenge in modeling of MHD flow with plasma discharge is the derivation of an expression for electrical conductivity.

Under the assumption of the low magnetic Reynolds number, no induced magnetic field is considered. Thus, the magnetic field remains time-invariant. In order to compute the magnetic field due to the permanent magnets, the potential theory for magneto static is used to derive the mathematical model to describe the magnetic field line.

2.6.1 Electrical conductivity

When the generalized Ohm's law is utilized, the explicit mathematical model to compute the electrical conductivity since it is known that the conductivity of the discharge region in the gas is non-uniform.

A phenomenological model for low-temperature surface plasma [22] is exploited in this work. It is assumed that the electrical conduction occurs by diffusion of the charged species.

The crucial issue with modeling of Magnetogasdynamics is to develop a mathematical model of the plasma discharge. It was found that the basic discharge structure is sustained by an electric field in all electronic collision ionizations [3].

The mathematical model of discharge was experimentally derived in terms of only the electric field strength and electric conductivity within the discharge domain [22].

$$\sigma(A, w, r, r_0, n) = \sigma_{\max} \exp\left[-w(r - r_0)^n\right] \qquad (2.41)$$

Where $\sigma_{\max}$ is the maximum magnitude of the electrical conductivity, w is the width of the discharge region, and r is the distance from the designated electrode location r0. The exponent n can be adjusted to describe the different discharge characteristics.

2.6.2 Magnetic dipole

Elementary magnetic fields are dipoles with a source (north) and sink (south) of magnetic field. Just as with electric fields, the superposition principle applies to magnetic fields. Mathematically, the solution needs to satisfy the following physical relation.

$$\nabla \cdot \vec{B} = 0 \tag{2.42}$$

Analogous to the potential flow theory, the magnets can be approximated as magnetic dipoles. By defining the magnetostatic potential as

$$\vec{B} \equiv \nabla \phi_B \tag{2.43}$$

The Laplace's equation can be obtained by substituting the magnetic field into the equation. In other words, magnetostatic scalar potential must be harmonic.

$$\nabla^2 \phi_B = 0 \tag{2.44}$$

The fundamental solution to the above equation for a point source in 3-D in Cartesian coordinate system is given as:

$$\phi_B = \frac{m_B}{|\vec{r} - \vec{r}_0|} = \frac{m_B}{\sqrt{(x-x_0)^2 + (y-y_0)^2 + (z-z_0)^2}} \tag{2.45}$$

As it was defined, magnetic flux can be found by taking the gradient of the magnetostatic potential.

$$\begin{aligned} \vec{B} = \nabla \phi_B &= \hat{i}\frac{m_B(x-x_0)}{\left[(x-x_0)^2 + (y-y_0)^2 + (z-z_0)^2\right]^{3/2}} + \hat{j}\frac{m_B(y-y_0)}{\left[(x-x_0)^2 + (y-y_0)^2 + (z-z_0)^2\right]^{3/2}} \\ &+ \hat{k}\frac{m_B(z-z_0)}{\left[(x-x_0)^2 + (y-y_0)^2 + (z-z_0)^2\right]^{3/2}} \end{aligned} \tag{2.46}$$

This is the magnetic flux produced by a source located at the point (x_0, y_0, z_0) assuming the sing of “m” is always positive. Magnetic flux with opposite effect can be also produced by a sink with the same strength. The potential and the flux have the exactly the same form with opposite sign of “m” and the different locations. Since both of them satisfy the equations above, these two fundamental solution can be added together to simulate the resultant effect due to dipoles according to superposition principle. Thus, the final form of magnetostatic potential is:

The magnetic field in 2D plane was considered. The distribution of the strength of the magnetic field can be found using 3D analytical model.

$$\phi_B = \frac{m_B}{\sqrt{(x-x_1)^2 + (y-y_1)^2 + (z_0 - z_1)^2}} - \frac{m_B}{\sqrt{(x-x_2)^2 + (y-y_2)^2 + (z_0 - z_2)^2}} \tag{2.47}$$

$$\begin{aligned} \vec{B} = \nabla\phi_B = \hat{i}&\left[\frac{m_B(x-x_1)}{\left[(x-x_1)^2 + (y-y_1)^2 + (z_0 - z_1)^2\right]^{3/2}} - \frac{m_B(x-x_2)}{\left[(x-x_2)^2 + (y-y_2)^2 + (z_0 - z_2)^2\right]^{3/2}}\right] \\ +\hat{j}&\left[\frac{m_B(y-y_1)}{\left[(x-x_1)^2 + (y-y_1)^2 + (z_0 - z_1)^2\right]^{3/2}} - \frac{m_B(y-y_2)}{\left[(x-x_2)^2 + (y-y_2)^2 + (z_0 - z_2)^2\right]^{3/2}}\right] \\ +\hat{k}&\left[\frac{m_B(z_0-z_1)}{\left[(x-x_1)^2 + (y-y_1)^2 + (z_0 - z_1)^2\right]^{3/2}} - \frac{m_B(z_0-z_2)}{\left[(x-x_2)^2 + (y-y_2)^2 + (z_0 - z_2)^2\right]^{3/2}}\right] \end{aligned} \tag{2.48}$$

Assuming that a 2-D plane right in the middle of the sink and the source ($z_1 = z_2$) is our computational domain, the analytical expression for the distribution of the magnetic flux in z-direction was found.

$$\vec{B}(x,y)=\hat{i}\left[\frac{m_B(x-x_1)}{\left[(x-x_1)^2+(y-y_1)^2+(z_0-z_1)^2\right]^{3/2}}-\frac{m_B(x-x_2)}{\left[(x-x_2)^2+(y-y_2)^2+(z_0-z_2)^2\right]^{3/2}}\right]$$
$$+\hat{j}\left[\frac{m_B(y-y_1)}{\left[(x-x_1)^2+(y-y_1)^2+(z_0-z_1)^2\right]^{3/2}}-\frac{m_B(y-y_2)}{\left[(x-x_2)^2+(y-y_2)^2+(z_0-z_2)^2\right]^{3/2}}\right] \tag{2.49}$$

CHAPTER 3

NUMERICAL METHODS

The governing equations obtained in Chapter2 need to be discretized both in time and space in order to obtain their solution. MHD fluid equations were discretized using conventional finite volume method with an upwinding scheme for convective flux. A multi-stage Runge-Kutta time stepping scheme was utilized to advance the solution in time. An upwinding scheme is necessary especially to model supersonic flow physics due to its directional dependent nature. Moreover, it is numerically important since it ensures the stability of the solution.

In addition to the MHD fluid equations, the space discretization of MHD electrodynamics equations can be achieved using Galerkin finite element method. The advantage of finite element method is that the higher accuracy in the solution can be attained relatively easily compared with the finite volume method by choosing different order of the shape function by which the solution is approximated.

3.1 Discretization of MHD flow equations

MHD fluid equations are solved on hybrid grid that consists of triangular and quadrilateral elements. The advantage of using unstructured grid is the ability to generate mesh over complex geometry. For the region where the high accuracy is required such as the inside of the boundary layer, the mapped or structured type grid can be used.

Higher-order accuracy in space discretization can be achieved by reconstruction of the solution variables at previous time step with linear extrapolation at the cell-interface. Since an upwind scheme, specifically flux difference splitting scheme, uses the state, solution variables, at both side of the cell-interface to evaluate the flux that is a function of the state of the flow right at the cell-interface.

3.1.1 Spatial discretization

$$\frac{\partial}{\partial t}\int_{\Omega}\vec{Q}d\Omega + \int_{\partial\Omega}\vec{H}\left(\vec{Q}\right)\cdot\vec{n}d\Gamma = \int_{\Omega}\vec{S}d\Omega \tag{3.1}$$

$$\delta\Omega\frac{\partial\vec{Q}}{\partial t} + \sum_{i}\left(\vec{E}n_x + \vec{F}n_y\right)_i\delta l_i = \delta\Omega\vec{S} \tag{3.2}$$

$$\vec{H}\left(\vec{Q}\right)\cdot\vec{n} = \left(\vec{V}\cdot\vec{n}\right)\begin{Bmatrix}\rho \\ \rho u \\ \rho v \\ \overline{E}_t + p\end{Bmatrix} + p\begin{Bmatrix}0 \\ n_x \\ n_y \\ 0\end{Bmatrix} \tag{3.3}$$

The flux normal to the cell-interface mathematically as shown above needs to be evaluated at the cell-interface between two cells. Flux split differencing was invented decades ago to overcome this problem and can be mathematically written as [25, 26]

$$\vec{H} = \frac{1}{2}\left[\vec{H}\left(\vec{Q}_R\right) + \vec{H}\left(\vec{Q}_L\right) - \left|\tilde{A}\right|\left(\vec{Q}_R - \vec{Q}_L\right)\right] \tag{3.4}$$

where $A \equiv \frac{\partial\vec{H}}{\partial\vec{Q}}$

The key to flux differencing scheme is how to evaluate the Jacobian matrix at the cell-interface since flux $\vec{H}$ needs to be evaluated on the cell-interface. Since the finite-volume method uses a piece wise constant approximation in each cell, different values in the solution can appear on the right hand and the left hand across the cell-interface. Roe suggested the averaging procedures based on the left and right state across the cell-interface [26]. Thus, the Jacobian matrix can be evaluated in terms of Roe-averaged variables. These procedures are briefly listed below. Eqns for Roe-averaged quantities [27]

$$\begin{aligned}
\tilde{\rho} &= \sqrt{\rho_L \rho_R} \\
\tilde{u} &= \frac{u_L + u_R \sqrt{\rho_R / \rho_L}}{1+\sqrt{\rho_R / \rho_L}} \\
\tilde{v} &= \frac{v_L + v_R \sqrt{\rho_R / \rho_L}}{1+\sqrt{\rho_R / \rho_L}} \\
\tilde{w} &= \frac{w_L + w_R \sqrt{\rho_R / \rho_L}}{1+\sqrt{\rho_R / \rho_L}} \\
\tilde{h}_0 &= \frac{h_{0L} + h_{0R} \sqrt{\rho_R / \rho_L}}{1+\sqrt{\rho_R / \rho_L}}
\end{aligned} \tag{3.5}$$

$$\begin{aligned}
\vec{H} &= \frac{1}{2}\left[\vec{H}\left(\vec{Q}_R\right)+\vec{H}\left(\vec{Q}_L\right)-\left|\tilde{A}\right|\left(\vec{Q}_R-\vec{Q}_L\right)\right] \\
&= \frac{1}{2}\left[\vec{H}\left(\vec{Q}_R\right)+\vec{H}\left(\vec{Q}_L\right)-\tilde{T}\left|\tilde{A}\right|\tilde{T}^{-1}\Delta\vec{Q}\right] \\
&= \frac{1}{2}\left[\vec{H}\left(\vec{Q}_R\right)+\vec{H}\left(\vec{Q}_L\right)-\left(\left|\Delta\tilde{F}_1\right|+\left|\Delta\tilde{F}_4\right|+\left|\Delta\tilde{F}_5\right|\right)\right]
\end{aligned} \tag{3.6}$$

3.1.2 Time integration

Although our interest is to obtain the steady state solution of the governing equations assuming that such solution exists, the unsteady term in the governing equation is kept and the solution was converged to the steady state flow conditions with time marching. In this way, hyperbolicity of a partial differential equation can be kept.

PDE can be converted into the ODE when the convective and diffusive flux terms and source terms are evaluated in terms of the solution variables obtained at the previous time step, which makes the scheme fully explicit.

Temporal discretiztion also introduces the numerical dissipation in addition to the numerical dissipation introduced due to the spacial discretization.

$$\delta\Omega \frac{\partial \vec{Q}}{\partial t} + \sum_{i} \left(\vec{E} n_x + \vec{F} n_y \right)_i \delta l_i = \delta\Omega \vec{S} \tag{3.7}$$

$$\delta\Omega_i \frac{\partial \vec{Q}}{\partial t} + R_i = 0 \tag{3.8}$$

Where $R_i = \sum_{j} \left(\vec{E}_i n_x + \vec{F}_i n_y \right)_j \delta l_j - \sum_{j} \left(\vec{E}_v n_x + \vec{F}_v n_y \right)_j \delta l_j - \delta\Omega_i \vec{S}_i$

$$\frac{\partial \vec{Q}}{\partial t} = -\frac{1}{\delta\Omega_i} R_i \tag{3.9}$$

The flux vector in x and y direction are split into the convective flux vector and viscous flux vector. The dot product of the flux vector evaluated at each cell-interface and unit normal vector to the interface forms the term on the right hand side of the equation as well as the volume integral of the source vector.

Fully explicit m-stage Runge-Kutta time-stepping scheme developed by Jameson [28] are shown below. It illustrates that the right hand side of the equation at each stage is just a function of the solution variables evaluated at the previous stage.

$$\begin{gathered} Q_i^{(0)} = Q_i^n \\ \vec{Q}_i^{(1)} = \vec{Q}_i^{(0)} - \alpha_i \frac{\Delta t}{\delta\Omega_i} \vec{R}_i^{(0)} \\ \vec{Q}_i^{(m-1)} = \vec{Q}_i^{(0)} - \alpha_{m-1} \frac{\Delta t}{\delta\Omega_i} \vec{R}_i^{(m-2)} \\ \vec{Q}_i^{(m)} = \vec{Q}_i^{(0)} - \alpha_m \frac{\Delta t}{\delta\Omega_i} \vec{R}_i^{(m-1)} \\ \vec{Q}_i^{(n+1)} = \vec{Q}_i^{(m)} \end{gathered} \tag{3.10}$$

The coefficient for each stage is given by the following formula.

$$\alpha_k = \frac{1}{m-k+1}$$

3.2 Discretization of MHD electromagnetic equations

Galerkin Finite Element method was exploited to spatially descretize the Poisson's equation of electric field. As a general remark, the finite element method have been extensively utilized in the field of structure dynamics. However, use of FEM is not limited only in this field. FEM can be applied to solve the general PDE problems with appropriate initial and boundary conditions such as Navier Stokes solver.

As the first step to the Galerkin solution of PDE, it needs to be recast into a weak integral form, which requires the definition of function spaces and associated norms.

In order to define the weak form of the boundary value problems, the test functions and the trial solutions need to be defined [29]. Its properties are mentioned briefly here. Test first collection of functions, denoted by ν , is composed of test functions and consists of all functions which are square integrable, have square integrable first derivatives over the computational domain Ω, and vanish on the Dirichelt portion, Γ_D, of the boundary. It can be mathematically written as,

$$\nu = \{ w \in \mathrm{H}^1(\Omega) | w = 0 \; on \; \Gamma_D \} \equiv \mathrm{H}^1_{\Gamma_D}(\Omega) \tag{3.11}$$

The trial solutions needs to satisfy the Dirichlet conditions on the boundary of the solution domain, Γ_D.

$$S = \{ u \in \mathrm{H}^1(\Omega) | u = u_D \; on \; \Gamma_D \} \equiv \nu + \{ \bar{u}_D \} \tag{3.12}$$

Where $\bar{u}_D$ is any function in $\mathrm{H}^1(\Omega)$ such that $\bar{u}_D = u_D$ on Γ_D.

$$-\nabla^2\phi = \rho_e(x, y) \tag{3.13}$$

The weighted residual formulation can be obtained by multiplying weighting function to the governing PDE and integrating over the whole domain.

$$-\int_\Omega w\nabla^2\phi d\Omega = \int_\Omega w\rho_e(x, y)d\Omega \tag{3.14}$$

Using the properties of gradient operator, the integral form of the governing equation can be rewritten as

$$-\int_\Omega (\nabla\cdot(w\nabla\phi) - \nabla w\cdot\nabla\phi)d\Omega = \int_\Omega w\rho_e(x, y)d\Omega \tag{3.15}$$

$$-\int_\Omega \nabla\cdot(w\nabla\phi)d\Omega + \int_\Omega \nabla w\cdot\nabla\phi d\Omega = \int_\Omega w\rho_e(x, y)d\Omega \tag{3.16}$$

Using Green-Gauss divergence theorem, the volume integral term can be written as the surface integral.

$$-\int_\Gamma w(\nabla\phi\cdot\vec{n})d\Gamma + \int_\Omega \nabla w\cdot\nabla\phi d\Omega = \int_\Omega w\rho_e(x, y)d\Omega \tag{3.17}$$

This step has a mathematically significant meaning. The regularity requirements on the test function and admissible solution are modified; the admissible function is only differentiated once and the test function must be differentiable.

By rearranging the equation above, the weak form of the governing equation can be written as the following.

$$\int_\Omega \nabla w\nabla\phi d\Omega = \int_\Omega w\rho_e(x, y)d\Omega + \int_\Gamma w\nabla\phi\cdot\vec{n}d\Gamma \tag{3.18}$$

The approximation of the solution can be achieved using the basis function. The linear basis function is used in this work. In other words, the linear variation of the solution variable in a cell is assumed. In Finite element method, the solution variable(s) can be computed at each node.

$$u^h(\vec{x}) = \sum_{A\in\eta|\eta_D} N_A(\vec{x})u_A + \sum_{A\in\eta_D} N_A(\vec{x})u_D(\vec{x}_A) \tag{3.19}$$

where N_A *the shape function associated with node number* A in the finite element mesh

In the Galerkin formulation, the arbitrary test functions, w^h, are defined such that

$$w^h \in \nu^h \equiv \underset{A\in\eta|\eta_D}{span}\{N_A\} \tag{3.20}$$

Thus, using these definitions, the equation can be written as

$$\sum_{B\in\eta|\eta_D} a(N_A, N_B)u_B = (N_A, s) + (N_A, h)_{\Gamma_N} - \sum_{B\in\eta_D} a(N_A, N_B)u_D(\vec{x}_B) \quad includeA \in \eta \mid \eta_D \tag{3.21}$$

where $1 \le A, B \le n_{np}$

This equation is written globally.

Each quadrilateral is mapped onto a canonical square with normalized local oordinates $(\xi, \eta) \in [-1,1] \times [-1,1]$ and the element shape functions are tensor products of those used in one dimension. Spacial variables and the solution variable are approximated in the same way.

$$\begin{Bmatrix} x \\ y \end{Bmatrix} = \sum_{a=1}^{4} N_a(\xi, \eta) \begin{Bmatrix} x_a \\ y_a \end{Bmatrix} \tag{3.22}$$

$$u^h(x, y) \equiv u^h(\xi, \eta) = \sum_{a=1}^{4} N_a(\xi, \eta) u_a \tag{3.23}$$

Now, the whole domain Ω needs to be descretize into the small domain Ω^e.

First, the local stiffness matrix and force vectors, which is a contribution from each element needs to be constructed.

$$K^e_{ab} = \int_{\Omega^e} \nabla N_a \cdot \nabla N_b d\Omega = a(N_a, N_b)_{\Omega^e} \tag{3.24}$$

$$f_a^e = (N_a, s)_{\Omega^e} + (N_a, h)_{\partial\Omega^e \cap \Gamma_N} - \sum_{b=1}^{n_{en}} a(N_a, N_b)_{\Omega^e} u_{D_b}^e \tag{3.25}$$

In order to solve the matrix equations, the sparse matrix solver was exploited to save the memory since most of the entries in the stiffness matrix are zero. The sparse matrix solver enables the algorithm to store only non-zero entries in stiffness matrix into the memory and to use them whenever needed just like accessing to the ordinary matrix. When the number of unknowns become large due to either/both increase in the number of equations to be solved or/and the number of nodes, an efficient way of utilizing computational resource available becomes crucial.

3.3 Evaluation of the first derivative

The solution to Poisson's equation is the electric potential. In order to obtain the electric field, the gradient of the electric potential needs to be evaluated. A derivative of the unknown at points can be recovered exploiting weighted residual methods once the unknown was computed.

The first derivative of the unknown in an element can be directly approximated by the nodal values of the first derivative of the unknown.

$$\frac{\partial \phi}{\partial s} \approx \sum_{i=1}^{r} N_i \left. \frac{\partial \hat{\phi}}{\partial s} \right|_i \tag{3.26}$$

The unknown, u can be approximated by the interpolation functions (shape function).

$$\phi \approx \sum_{i=1}^{r} N_i \phi_i \tag{3.27}$$

Let us take a derivative of both sides of the equations.

$$\frac{\partial \phi}{\partial s} \approx \sum_{i=1}^{r} \frac{\partial N_i}{\partial s} \hat{\phi}_i \tag{3.28}$$

By equating the two equations above,

$$\sum_{i=1}^{r} N_i \left.\frac{\partial \hat{\phi}}{\partial s}\right|_i = \sum_{i=1}^{r} \frac{\partial N_i}{\partial s} \hat{\phi}_i \tag{3.29}$$

Weighting this relation with shape-functions W^i

$$\int_\Omega W^i N^j d\Omega \left.\frac{\partial \phi}{\partial s}\right|_j = \int_\Omega W^i \frac{\partial N^j}{\partial s} d\Omega \hat{\phi}_j \tag{3.30}$$

$$\sum_{i=1}^{r} N_i \left.\frac{\partial \hat{u}}{\partial s}\right|_i = \sum_{i=1}^{r} \frac{\partial N_i}{\partial s} \hat{u}_i \tag{3.31}$$

The Galerkin weighted residual method was used

$$[M]\left\{\frac{\partial \phi}{\partial s}\right\} = \int_\Omega N^i N^j d\Omega \left.\frac{\partial \phi}{\partial s}\right|_j = \int_\Omega N^i \frac{\partial N^j}{\partial s} d\Omega \hat{\phi}_j \tag{3.32}$$

Thus, now the problem is reduced to the matrix inversion. Since the mass matrix contains the non-zero off diagonal entries, the simultaneous system of equations needs to be solved. In this program, the preconditioned conjugate gradient (PCG) solver was used to achieve this operation.

FEM uses the element based data structure while FVM for flow solver uses the edge based data structure. This difference is simply due to the difference in the way to solve governing equations.

FVM requires the evaluation of flux terms at the cell interfaces, which is an ultimate problem. Since this flux needs to be conserved when the control volume is taken at a cell-interface, the flux in and out to the neighboring cell is the same in magnitude and opposite in its sign. Thus, flux needs to be computed once for each cell-interface. On the other hand, The finite element code was developed based on the weak form of the PDE. In order to solve the equations on the same mesh as the flow solver uses, the code was designed in a way that it can handle hybrid mesh that consists of triangular and quadrilateral elements. Though the construction of local stiffness matrix slightly differs due to the difference between the number of nodes in each element, the outline of the procedure is the same.

The finite element method requires the operation of inverting stiffness matrix whose size is square of number of unknowns. Thus, the majority of computational time is spent on this operation. Furthermore, the stiffness matrix is a sparse matrix. In other words, most of the entry of this matrix is zero.

3.4 Mesh

The actual governing equations solved in this code keep the unsteady term and march down to the solution with the same procedure as the unsteady calculations.

The Navier Stokes equations were solved until it converges with the electrodynamics turned off. This converged solution was used as an initial condition to simulate the interaction of electromagnetic field and aerodynamics.

3.5 Boundary conditions

3.5.1 Viscous surface

No-slip condition for velocity is exploited at the surface.

$$u_w = v_w = 0 \tag{3.33}$$

Either the temperature of the wall or the condition of the heat flux can be also specified. Here, the adiabatic wall condition is used.

$$\vec{q} \cdot \vec{n} = (k \nabla T)\vec{n} = 0 \tag{3.34}$$

The pressure on the surface (pb) is determined by linear extrapolation.

The normal gradient of the pressure is zero.

$$p_b = p_1 - (p_2 - p_1)/2 \tag{3.35}$$

3.5.2 Characteristic inflow/outflow

The inflow/outflow boundary conditions are cell-face type boundary conditions. In the far field, the velocity normal to the far boundary (pointing out of the grid) and the speed of sound are obtained from two locally 1-d Riemann invariants:

(Provide more discussions regarding with the physical meanings of it.)

$$R_n^{\pm} = \vec{v} \cdot \vec{1}_n \pm \frac{2a_{face}}{\gamma - 1} \tag{3.36}$$

The normal velocity and speed of sound are determined from

$$\begin{aligned} \bar{u}_{face} &= \frac{1}{2}\left(R_n^+ + R_n^-\right) \\ a_{face} &= \frac{\gamma - 1}{4}\left(R_n^+ - R_n^-\right) \end{aligned} \tag{3.37}$$

The sign of the normal velocity determines whether the condition is at inflow (vn<0) or outflow (vn>0). The entropy p/ρ^{γ} is determined using the value from outside the domain for inflow and from inside the domain for outflow. The entropy and speed of sound are used to determine the density and pressure on the boundary:

$$\begin{aligned} \rho_{face} &= \left[\frac{\left(a_{face}\right)^2}{\gamma s_{face}}\right]^{\frac{1}{\gamma - 1}} \\ p_{face} &= \frac{\rho_{face}\left(a_{face}\right)^2}{\gamma} \end{aligned} \tag{3.38}$$

CHAPTER 4

CODE VALIDATIONS

The validation of the finite volume code developed in CFD lab was performed against the analytical solution for Poisulle flow. Analytical solution to the Poisulle flow is one of a few exact solutions that can be attained. In order to investigate the capability of the code, a more complex problem was selected as another test case for the flow solver. The experimental result for the internal flow over turbine cascade was used for the comparison.

Finite element Poisson's equation solver for the computation of electric potential and electric field were also validated against the exact solution. For this test case, Laplace's equation of electric potential was used.

4.1 Poiseuille flow

Isothermal, laminar flow (ReH<~1000) of an incompressible Newtonian fluid in a long two-dimensional channel with height H is considered. The driving force to the flow in the channel is the applied pressure gradient between the inlet and the exit of the channel. The exact solution can be obtained by assuming the steady and fully developed flow between two plates. It implies that the velocity profile does not change along the direction of the flow. Therefore, an arbitrary location along the direction of the flow can be selected to sample the velocity profile. The derivation of the exact solution to this problem is readily available in any fluid dynamics textbooks [30].

$$u = \frac{1}{2\eta}\frac{dP}{dx}\left[y^2 - \left(\frac{H}{2}\right)^2\right] \tag{4.1}$$

The x-component of the velocity was normalized by the maximum value of the x-velocity at the middle of the channel section. The normalized velocity profile is a function of the normalized distance from the middle point in the channel.

$$u_{\max} = -\frac{1}{2\eta}\frac{dP}{dx}\left[\left(\frac{H}{2}\right)^2\right] \tag{4.2}$$

$$\frac{u}{u_{\max}} = \left[4\left(\frac{y}{H}\right)^2 - 1\right] \tag{4.3}$$

4.1.1 Problem setup

A 15 by 1 rectangular domain was considered since it takes some distance for the flow to fully develop unlike the analytical solution. A mapped grid with quadrilateral elements was exploited to simulate the channel flow. For this reason, a large aspect ratio was selected.

4.1.2 Boundary conditions

Three types of boundary conditions were used for this problem. On the wall, the non-slip condition was used to assure the velocity on the wall to be zero. Both at the inlet and outlet, the different values of the pressure were assigned as a boundary condition. This pressure difference between the upstream and the downstream enforce the medium to flow. At the inlet, the characteristic type of boundary condition was used. The outflow boundary condition was used at the outlet.

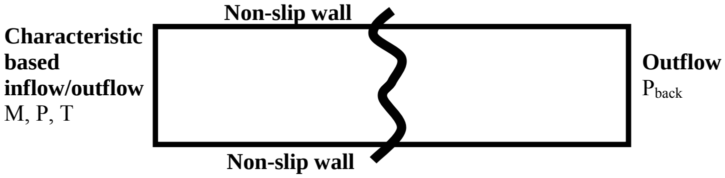

Figure 4.1. Boundary conditions

4.1.3 Results

Velocity profile between two plates was obtained from the numerical result. The x component of velocity and y coordinate were normalized by the maximum velocity of the profile and the Height of the channel, respectively. As shown in Figure 4.2, reasonable agreement between the numerical and analytical solutions is observed. It was also observed that there is slight error in profile. This is perhaps due to treatment of the boundary conditions at the wall. The velocity at the wall was a small finite value, which results in slight offset from the analytically obtained profile. In this work, it was judged that this degree of disagreement was acceptable.

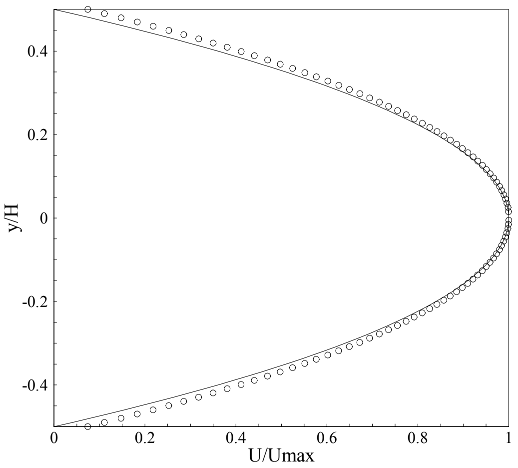

Figure 4.2. Velocity profile

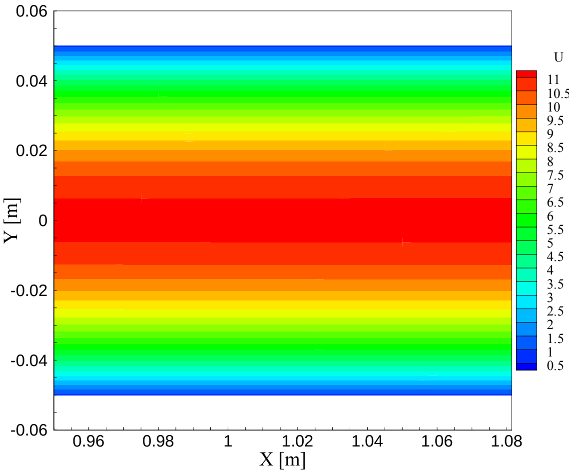

Figure 4.3. Contour of x-component of velocity

4.2 Turbine cascades

In order to validate the finite volume solver for relatively complicated problem, a transonic flow over the turbine cascade was selected. This benchmark case validates capability of the code of computing subsonic low Mach number to supersonic high Mach number range. The experimental data was obtained in AGARD [31].

4.2.1 Problem setup

The dimension of the inlet and outlet lengths are the exactly the same as the pitch given in the test case. The top and bottom boundary are identical to each other so that the periodic boundary condition can be imposed.

The hybrid mesh was constructed by using AFLR2. It consists of two types of elements or cells. Quadrilateral elements near the wall surface were used to more accurately capture features of boundary layer. It allows us to cluster the grid toward the wall uniformly along the contour. Furthermore, the lines can be orthogonal to the wall surface, which is advantageous to evaluate the velocity gradient normal to the wall. Triangle elements were used in most of the domain away from the near-boundary region was used.

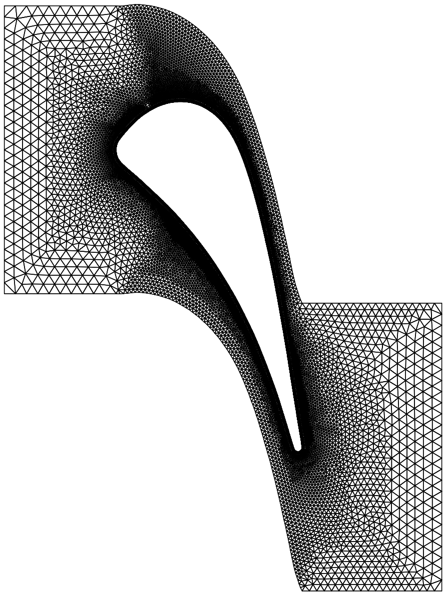

Figure 4.4. Grid

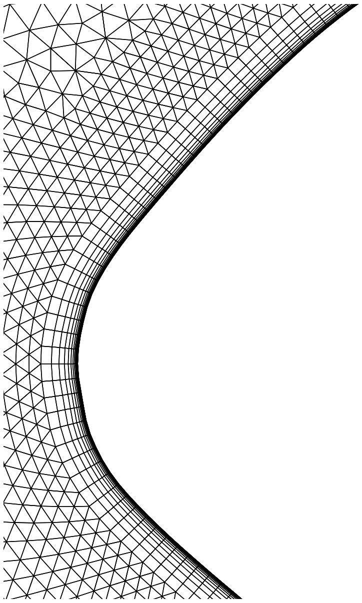

Figure 4.5. B.L. mesh at leading edge

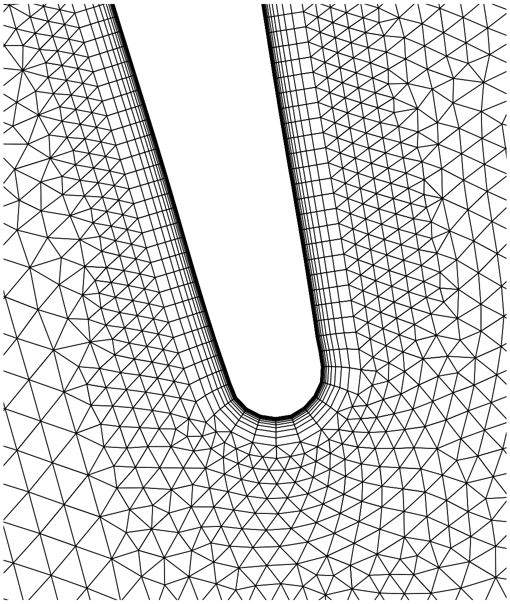

Figure 4.6. B.L. mesh at trailing edge

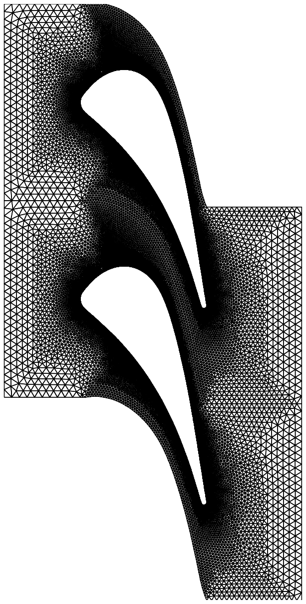

Figure 4.7. Periodicity of geometry

Table 4.1 Input parameters

inlettotaltemperature	$T_{01} \cong 278K$
inletTotal Pr *essure*	$P_{01} = 1.3to2.3bar$
Re *ynoldsNumber*	$increasewithM_2$
InletFlowAngle	$\beta_1 = 1.9^\circ\,(fro\max ialdirection)$

4.2.2 Boundary conditions

The boundary conditions need to be assigned to satisfy all the test conditions. The numerical aspects of boundary conditions are discussed in Chapter3. The appropriate boundary conditions for this case are listed below. The inlet pressure and Mach number were specified according to the experimental condition. The outflow boundary condition where the back pressure was specified was used at the outlet. On the surface of the turbine cascade, non-slip condition where the velocity at the surface is zero was used. The flow structure around the stuck of the cascades is periodic due to the periodic geometry. Thus, the periodic boundary condition was used to save the computational effort.

4.2.3 Data reduction

Once the flow field variables were obtained, the static pressure distribution over the blade contour was reduced to the isentropic Mach number along the chord length. This data reduction can be done using isentropic relationships.

$$\frac{p_t}{p_s} = \left[1 + \frac{\gamma - 1}{2} M_s^{\,2}\right]^{\frac{\gamma}{\gamma - 1}} \tag{4.4}$$

$$\left(\frac{p_t}{p_s}\right)^{\frac{\gamma - 1}{\gamma}} = 1 + \frac{\gamma - 1}{2} M_s^{\,2} \tag{4.5}$$

$$M_s = \sqrt{\left(\frac{2}{\gamma - 1}\right)\left[\left(\frac{p_t}{p_s}\right)^{\frac{\gamma - 1}{\gamma}} - 1\right]} \tag{4.6}$$

To determine the value of static pressure at the outlet for a boundary condition, an isentropic relation was used with a give value for the isentropic Mach number $M_{3,is}$ for each test case in [31].

$$\frac{p_{0,3}}{p_3} = \left[1 + \frac{\gamma - 1}{2} M_{3,is}{}^2\right]^{\frac{\gamma}{\gamma-1}} \tag{4.7}$$

$$\frac{p_3}{p_{0,3}} = \left[1 + \frac{\gamma - 1}{2} M_{3,is}{}^2\right]^{-\frac{\gamma}{\gamma-1}} \tag{4.8}$$

In order to account for the total pressure loss in the flow across the cascade, the total pressure loss was assumed.

$$\frac{p_{03}}{p_{01}} = 0.92 \tag{4.9}$$

$$\begin{aligned} p_3 &= p_{0,1}\left(\frac{p_{0,3}}{p_{0,1}}\right)\left(\frac{p_3}{p_{0,3}}\right) = \left(\frac{p_{0,3}}{p_{0,1}}\right)\left[1 + \frac{\gamma - 1}{2} M_{3,is}{}^2\right]^{-\frac{\gamma}{\gamma-1}} \\ &= (177700Pa)(0.92)\left[1 + \frac{1.4 - 1}{2} 1.43^2\right]^{-3.5} \\ &= (177700Pa)(0.92)(0.27709) \\ &= 45300Pa \end{aligned} \tag{4.10}$$

4.2.4 Results

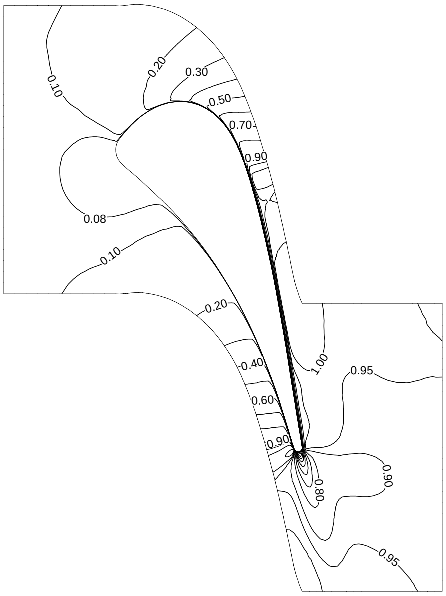

Figure 4.8. Mach number contour

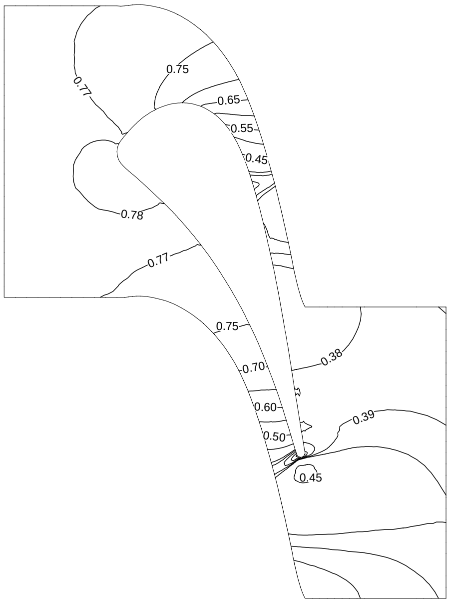

Figure 4.9. Static pressure contour

Figures4.8 and 4.9 show the unique features of transonic internal flow. Due to this specific cascade configuration, the region between two cascades is just like a converging-diverging nozzle as shown in Figure4.7. The flow over the suction side of the cascade experiences rapid acceleration from the low speed to the sonic speed. For this particular case, the pressure ratio of inlet to the outlet was not significant enough for the flow to be further accelerated to the supersonic in the downstream.

Figur4.9 depicts the non-dimensionalized static pressure distribution. Continuous decrease in static pressure from the stagnation point at the nose to the outlet displays the flow is continuously expanded with favorable pressure gradient. It should be noted that in the region on the pressure side of the blade near the trailing edge, iso-pressure lines are becoming close together. As the back pressure is decreased, the shock wave is eventually formed in this region, which will create the adverse pressure gradient upstream of the shock location. This may cause shock induced separation.

4.3 Validation of FEM solver

To validate the finite element Poisson's solver, conducting cylinder of radius, a, and surrounded concentrically by conducting cylindrical shell of inner radius, b, was computed for the given value of the charge per unit length. Because of the symmetry of the domain, the problem can be modeled by one dimensional Laplace's equation written in the polar coordinate.

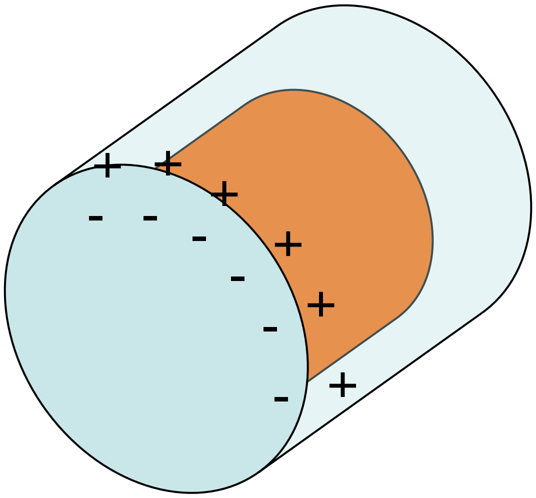

Figure 4.10. Parametric view of cylindrical capacitor

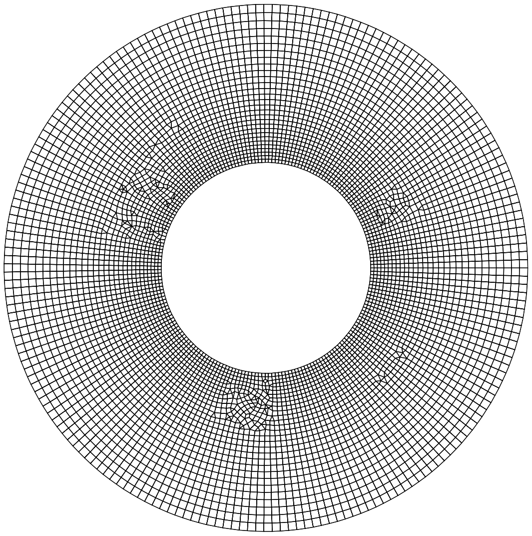

Figure 4.11. Computational domain between two cylinders

Analytical solution can be easily derived using Gauss's law considering the domain between cylinders. Electric potential at any radius between cylinders can be computed by integrating the electric field taking the reference voltage.

4.3.1 Results

Figure 4.12 depicts excellent agreement with the analytical solution for the electric potential. It ensures the accurate computation of the distribution of electrical potential in the computational domain. Furthermore, contour of the electric potential between two cylindrical plates are shown in Figure 4.13. As assumed in the derivation of the analytical solution, there is not variation of the electric potential in tangential direction. Furthermore, the electric field is defined as a gradient of electric potential. Thus, every iso-potential line is normal to arrowed electric field lines as shown in Figure 4.13.

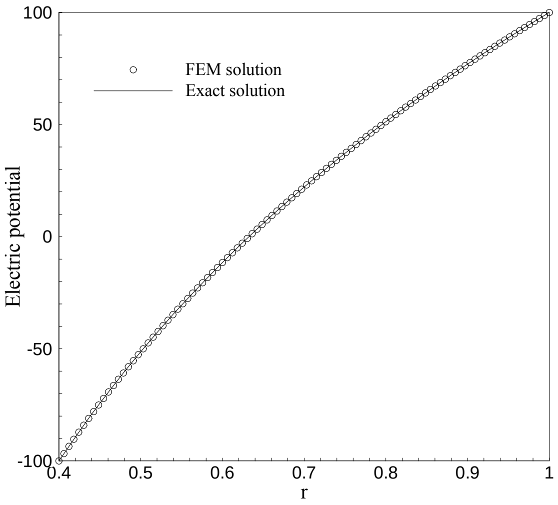

Figure 4.12. Electric potential in radial direction

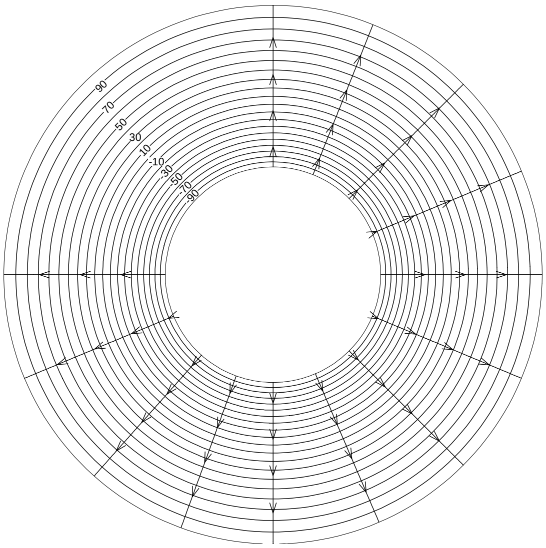

Figure 4.13. Contour of electric potential and electric field lines

CHAPTER 5

NUMERICAL SUTYD OF MHD EFFECTS

5.1 Hartmann flow

MHD channel flow first investigated by Hartmann in 1930s was considered. MHD effect on the velocity profile of the channel flow due to externally applied uniform magnetic field was of particular interest. An external electric field was turned off to see the pure effect of the magnetic field on the electrically conducting fluid. Altered velocity profile was compared with that obtained in the classical Poiseuille flow problem in Chapter4. Furthermore, effects of the non-dimensional MHD parameters were discussed with simulation results.

5.1.1 Problem setup

The same geometry as the Poiseuille flow problem was considered. The height and length of the channel were 0.1 and 1 meter, respectively. A span of the channel was assumed to be infinitely long so that there is no variation of velocity profile in span wise direction between two side walls. Under this assumption, a two dimensional model is valid.

Uniform time-invariant magnetic field was applied in a transverse direction to that of flow shown in Figure 5.1. Since no electric field was present in the flow for the first simulation, the current was produced by the average velocity and the magnetic flux density according to the generalized Ohm’s law. Thus, body force acting on the flow is purely due to the magnetic field.

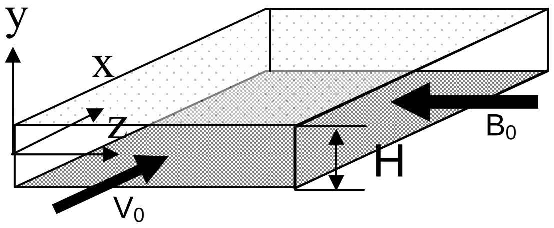

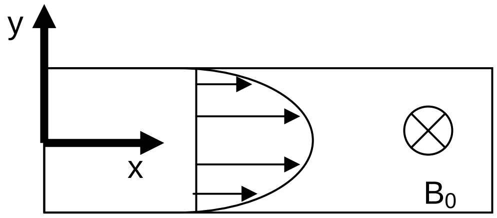

Figure 5.1 Channel flow

Figure 5.2. Side view of the channel flow

The boundary conditions for the flow variables were specified in the same way as the Poiseuille flow since the induced magnetic field was not computed. The inlet and outlet flow conditions are also the same as the Poissuile flow.

5.1.2 Results and discussions

The flow under the influence of the magnetic field was computed. Results are presented in a dimensional form. Figure 5.3 shows the velocity profile sampled at the location one meter away from the inlet for different strength of magnetic flux density. The electrical conductivity was assumed to be uniform with a constant value of 0.1 [mho].

Figure 5.3 clearly displays that a velocity profile becomes flattened as a value of magnetic flux density increases. This flattening becomes more apparent near the center of the channel where the maximum speed in the flow direction is observed. This is also obvious from the mathematical expression of the Lorentz force, a cross product of the average flow velocity and magnetic flux density. The larger the magnitude of the velocity is with the constant magnetic flux density, the more MHD effect can be observed. Therefore, flattening in the velocity profile at the wall is almost negligible since the speed of the flow is very small compared with the flow in the middle of the channel.

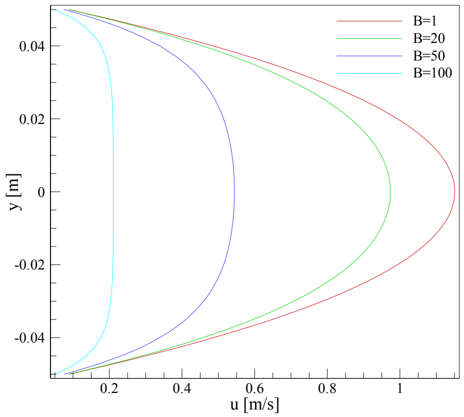

Figure 5.3. Velocity profile for B=1, 20, 50, and 100 [T] with σ=0.1 [mho]

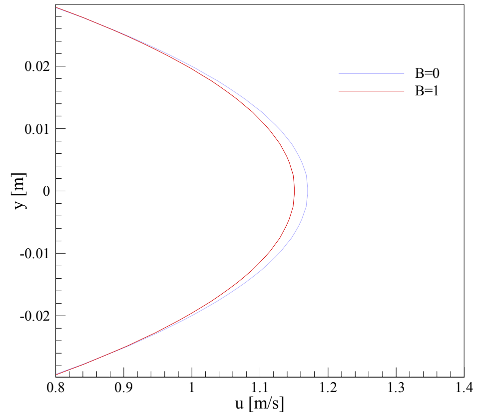

Figure 5.4. Comparison of velocity profile with σ=0.1 [mho]

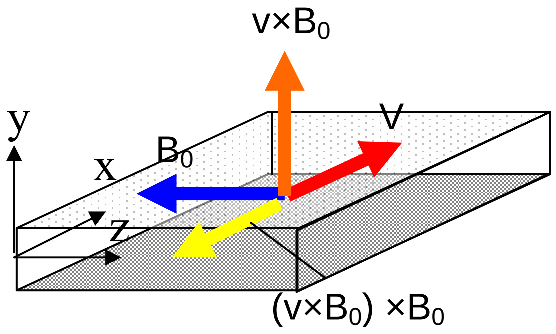

Figure 5.5. Magnetic pressure

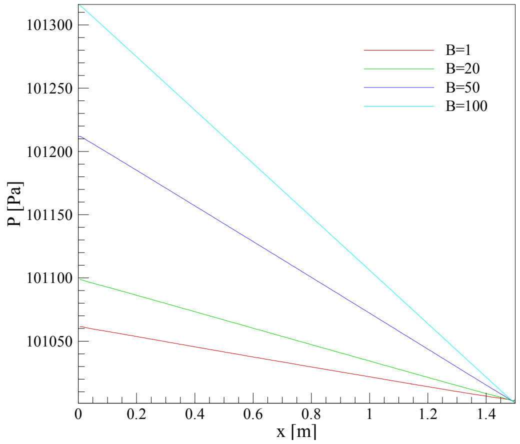

Figure 5.6. Change in pressure along x-axis for B=1, 20, 50, and 100 [T]

The direction of the body force acting on the flow is against the flow, which results in resisting force to the flow. This is always the case with this type of configuration shown in Figure5.5. Even when the polarity of the magnetic field is changed, in other words, the direction of magnetic field is in positive z-direction, the body force acting on the flow remains the same. This resisting effect to the flow is called magnetic pressure, which forces flow to slow down.

By keeping the back pressure constant, inlet pressure varies assuming that there is a control valve upstream of the inlet. It can be observed that increase in the magnitude of magnetic flux density increases static pressure at every location along the channel as shown in Figure 5.6.

Furthermore, the value of magnetic flux density used here perhaps cannot be realized except the case for 1 Tesla. Most of rare earth magnets have the magnitude of less than one Tesla. Figure 5.4 illustrates that an effect of magnetic pressure is negligible within this range of magnetic field. This fact is advantageous for flow acceleration.

5.2 Hartmann flow with uniform electric field

In the previous simulation, an effect of the magnetic field was demonstrated by applying only the time-invariant uniform magnetic field, which caused deceleration of the flow. On the other hand, great interest of many engineering applications is to accelerate the flow. It can be realized adding uniform electric field.

5.2.1 Problem setup

In this simulation, effects of externally applied uniform electric field in addition to uniform magnetic field were investigated in the channel flow. All the conditions were kept the same as the previous simulation of Hartmann flow. Only change made was that externally applied uniform electric field is present between the two plates in the channel. The cathode was placed on the top and the anode was placed to the bottom of the channel, which will create the uniform electric field across the two plates.

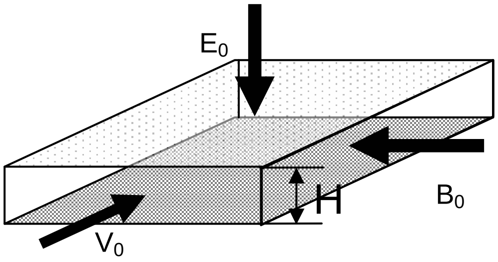

Figure 5.7 Channel flow

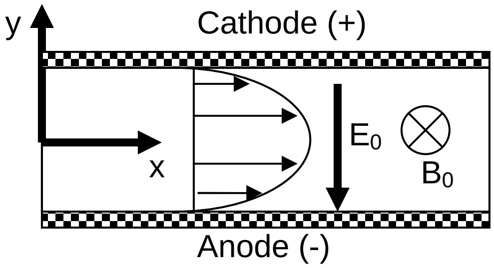

Figure 5.8. Side view of the channel flow

5.2.2 Results and discussions

Velocity profiles were obtained at the same location along the channel for different values of electrical field with a constant value of magnetic flux density. The electrical conductivity was also assumed to be uniform and constant. The strength of the electric field is determined by the applied voltage across the electrodes and distance between them. Figure 5.9 shows that as the strength of the electric field increases, the flow acceleration becomes more significant, which results in the stretched profile in the direction of the flow.

Pressure distribution corresponding to different strength of electric field along the channel from the inlet to the exit was shown in Figure 5.10. It illustrates that negative pressure gradient start increasing from the favorable pressure gradient that causes the fluid in motion. Further increase in the magnitude of electric field causes the pressure gradient to be positive or adverse pressure gradient. Since the simulation result shows the flow is still in the original direction of the flow, this adverse pressure gradient is overcome by Lorentz force acting on the flow.

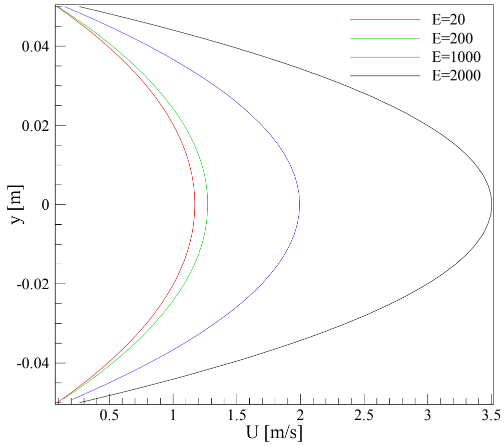

Figure 5.9. Velocity profile for E= 20, 200, 1000, and 2000 [V/m] at x=1.0 [m] with σ=0.1 [mho] and B=1 [T]

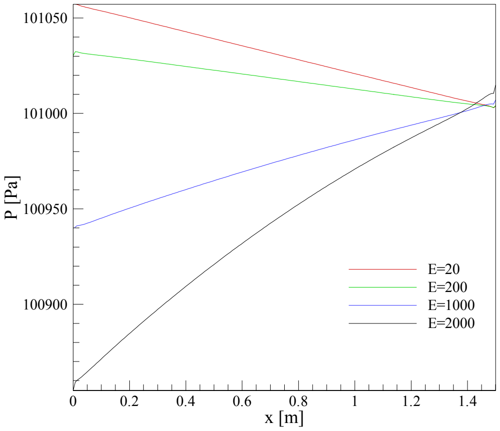

Figure 5.10. Change in pressure along x-axis for E=20, 200, 1000, and 2000 [V/m] with σ=0.1 [mho] and B=1 [T]

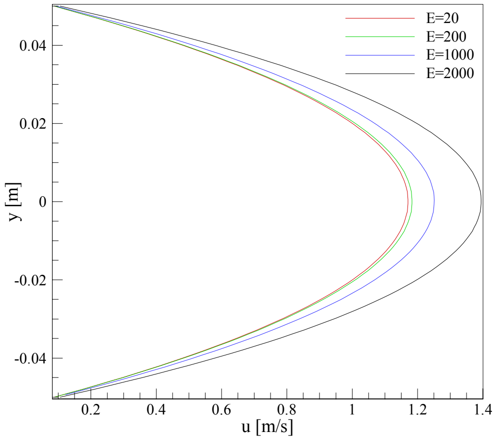

Figure 5.11. Velocity profile for E= 20, 200, 1000, and 2000 [V/m] at x=1.0 [m] with σ=0.01 [mho]

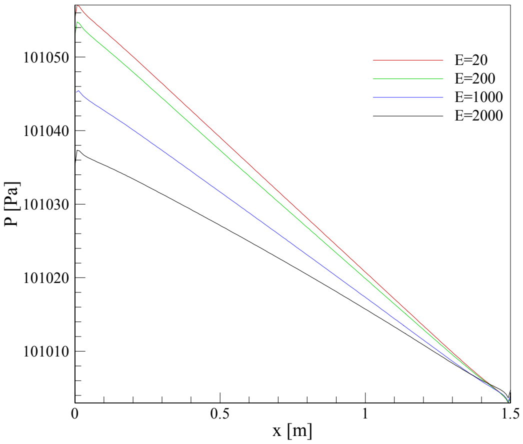

Figure 5.12. Change in pressure along x-axis for E=20, 200, 1000, and 2000 [V/m] with σ=0.01 [mho]

The same analysis was performed with a decreased value of electrical conductivity shown in Figure 5.11 and Figure 5.12. All other conditions were kept the same. Effects of electrical field on velocity profile and pressure distribution become less significant due to decrease in current driven by the electric field. Indeed, the pressure gradient remains negative for the same range of electric field as the previous case.

5.3 MHD channel flow with non-uniform electromagnetic field

In the previous simulations, uniform electric field was assumed. However, this particular configuration of electrodes pair many not be realized for certain applications such as boundary layer control of the external flow. In this case, since the two electrodes pair needs to be located on the same surface of the body, the electric field becomes concentrated only in the vicinity of these electrodes. This raises the need to compute externally applied electric field.

5.3.1 Problem setup

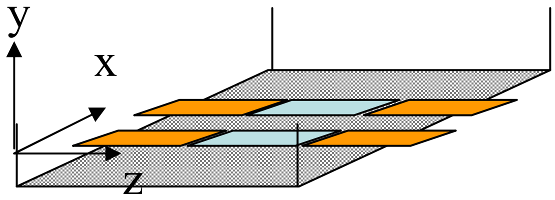

Figure 5.13. Localized electromagnetic field

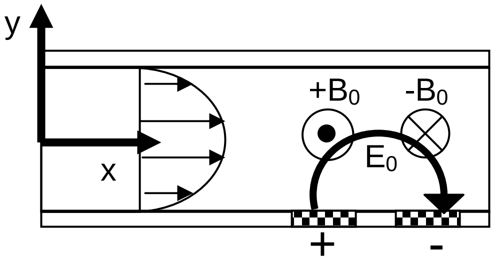

Figure 5.14. Side view of localized electromagnetic field

An electrodes pair was located on the bottom wall of the channel at the location, 0.5 meter away from the inlet. Two electrodes are 0.01 meter apart and the point where the half of distance from each other coincides with the point 0.5 meter away from the inlet. Along with change of the configurations of position of the electrodes pair, a constant uniform magnetic field cannot be used to achieve acceleration of the flow above the two electrodes. The current flows from the cathode surface and goes back into the anode. In the vicinity of the cathode, the current is in the positive up direction while it is in the downward direction. This polarity in the direction of the current will create the polarity of the body force acting on flow if the polarity of the magnetic field is the same both above the cathode and the anode.

In order to achieve continuous acceleration of the flow, by keeping the same configuration of the electrodes pair, there must be polarity in the externally applied magnetic field on the cathode and the anode. This arrangement is depicted in Figure 5.13.

For this simulation, instead of assuming the uniform magnetic field, two pairs of dipole magnetic potential in three dimensional were used to compute the magnitude of magnetic field flux density penetrating the domain of the simulation.

5.3.2 Results and discussions

Since the electric field and magnetic field are no longer uniform constant, they need to be computed. Electric field produced by a pair of electrodes was computed and visualized by the electric field lines. Figure 5.15 shows that the electric potential decades rapidly with a distance from electrodes surface. It implies that strength of the electric field is substantial only in the vicinity of the electrodes.

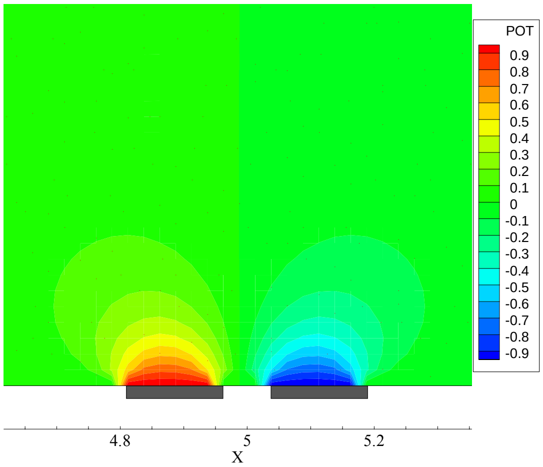

Figure 5.15. Contour of electric potential

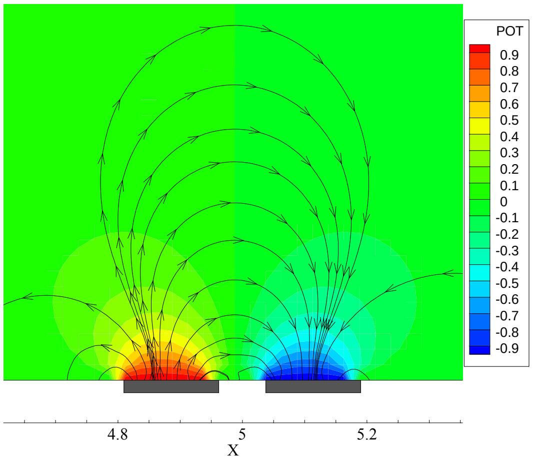

Figure 5.16. Electric field lines

The magnetic field that is normal to the computational domain was computed using two pairs of di-poles derived from the potential theory. The three dimensional mathematical expression was used to calculate the strength of the field normal to the domain. In other words, only the z-component of the magnetic field produced by two pairs of magnets need to be obtained since other components will not contribute to body force production.

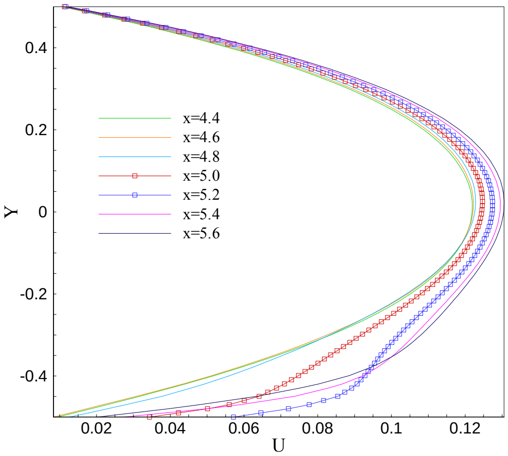

Figure 5.17. Velocity profile sampled at different locations

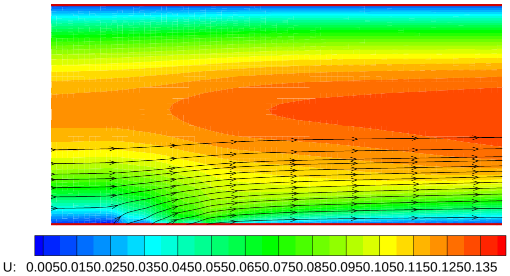

Figure5.18. Contour of x-component of velocity and streamlines

Figure 5.17 shows the altered velocity profile sampled at different locations due to the presence of electric field and magnetic fields. The sampling locations are shown in Figure 5.18. The velocity profile upstream of the cathode location is not affected by the field. However, the velocity profile sampled directly above the location of the cathode experiences significant change in its profile. Flow is further accelerated near the anode region. The change in velocity profile becomes less significant downstream of the anode.

5.4 MHD flow control over a circular cylinder

In the previous simulations, MHD effects on low speed flow were investigated using the channel flow problems. However, a question arises whether or not appreciable alternation of the flow field in higher Reynolds number regime can be observed. In order to answer this question, the subsonic flow over the cylinder was considered.

5.4.1 Problem setup

A cylinder with a diameter of 0.5 [m] was considered. The free stream Mach number was kept 0.5. Three electrodes were placed apart by 30 degrees from each other at the top and bottom of the cylinder. Again, the polarity of electrodes was decided in such a way that it produced the acceleration of flow.

Only the magnitude of the applied voltage was varied from 200 volts to 1200 volts to examine change in flow field near the cylinder. The magnetic flux density that characterizes the strength of the magnetic field was kept constant of 1 Tesla. It was also assumed that the plasma gas has a uniform property of the electrical conductivity and constant value of 0.1 [mho].

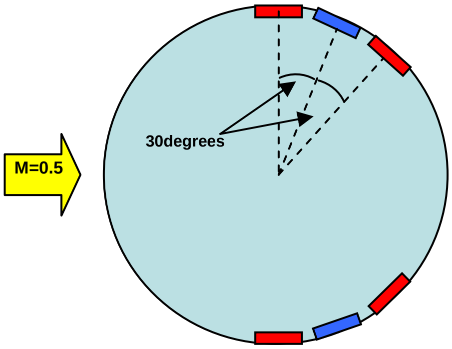

Figure 5.19. Arrangement of electrodes

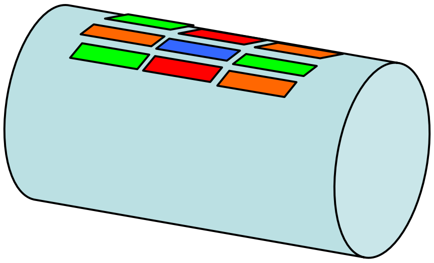

Figure 5.20. Arrangement of electrodes and magnets

5.4.2 Results and discussions

The same magnitude with the opposite polarity of voltage was applied to electrodes. Figure 5.21 depicts the electric potential produced in the vicinity of these electrodes. For this particular case, 200 volts was applied to each electrode. The blue region shows the negative electric potential in Figure 5.21. Figure 5.22 illustrates the electric field lines produced by these electrodes. Just like a channel flow case, the directions of the electric field and the magnetic filed are essential to obtain a desired effect, either acceleration of the flow or deceleration of flow. Once the polarity of electrodes are determined, that of magnets can be determined shown in Figure 5.23.

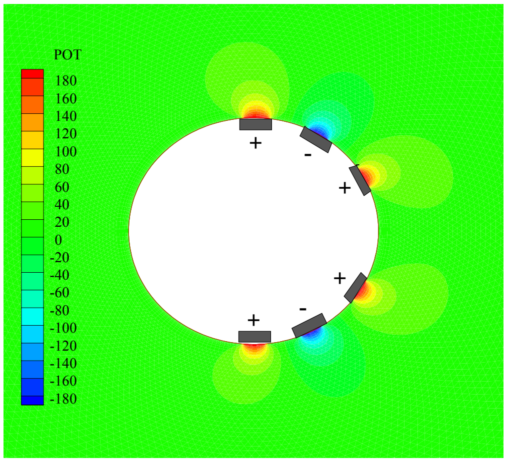

Figure 5.21. Contour of electric potential

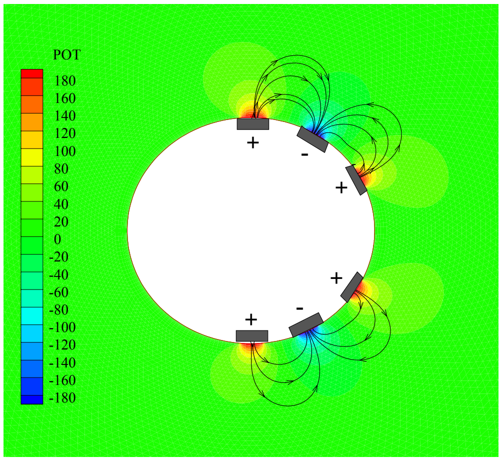

Figure 5.22. Electric field lines

As shown in Figure 5.23, the magnetic flux density is fixed to be a constant of 1 Tesla. The red region means that the direction of the magnetic field is in positive z-direction which is out from the page. The blue region is the opposite direction.

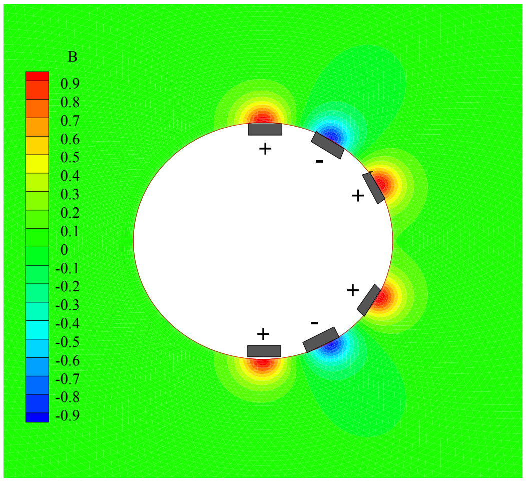

Figure 5.23. Contour of z-component of magnetic flux density

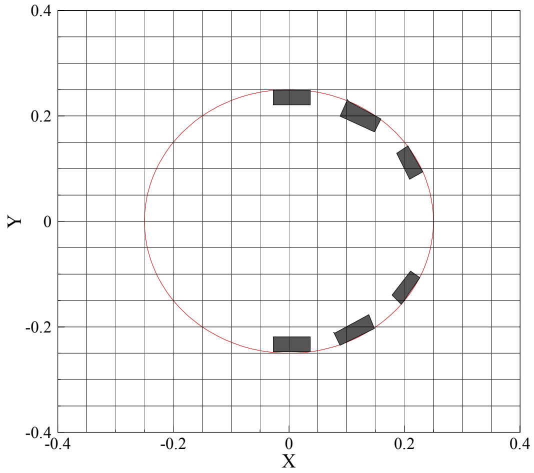

Figure 5.24. Location of electrodes

A qualitative analysis can be made from the following pressure contours for different magnitudes of the applied voltage. Results were plotted in the same scale for all cases. As the magnitude of the applied voltage increases from 200 volts, change in pressure contour near the top and the bottom portion of the cylinder was observed. The noticeable change was that the minimum pressure that occurs in the expansion region becomes larger as the applied voltage was increased. The same phenomenon was observed even in Figure 5.10 in the channel flow. Favorable pressure gradient initially present eventually turned to an adverse pressure gradient.

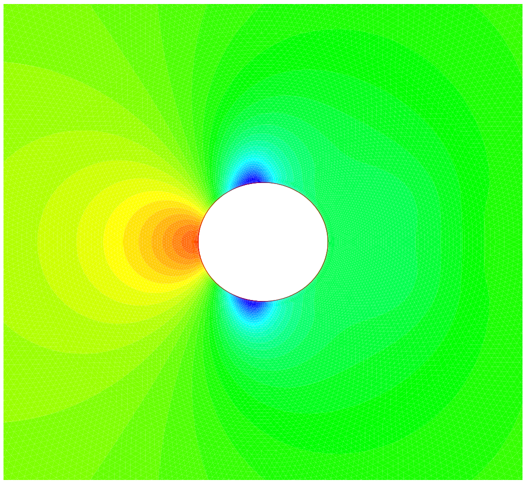

Figure 5.25. Applied voltage: 200 [V]

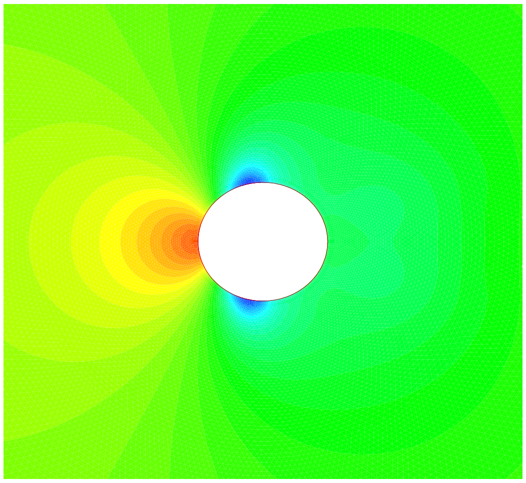

Figure 5.26. Applied voltage: 500 [V]

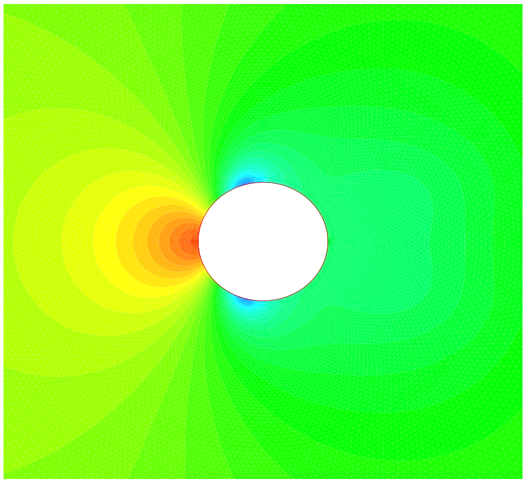

Figure 5.27. Applied voltage: 800 [V]

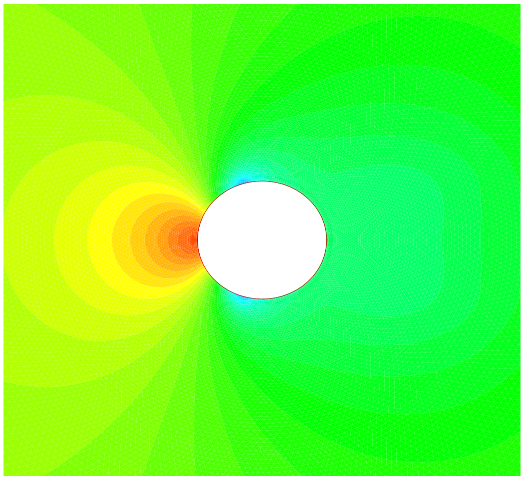

Figure 5.28. Applied voltage: 1000 [V]

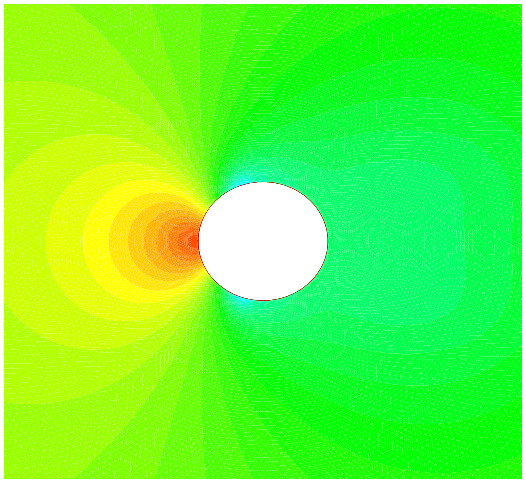

Figure 5.29. Applied voltage: 1200 [V]

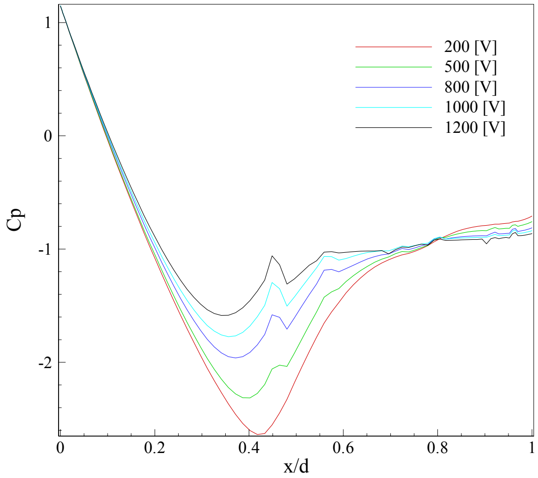

Figure 5.30. Pressure coefficient distribution

Figure 5.30 also illustrates that decrease in pressure distribution along the top surface of the cylinder becomes less significant. For lower applied voltage, rate of decrease in pressure in the expansion region is much higher than that for higher voltage. Furthermore, rate of increase in pressure in the compression region for lower voltage is also much higher.

It should be also noted from Figure 5.30 that the location where the lowest pressure takes place shifts toward the front as the applied voltage was increased. It indicates that the flow expansion region became shorter and the flow compression region became longer instead. One possible reason for this is that deflection of flow due to the first electrode mounted at x=0 location acts as a wedge like obstacle in the flow. As noted in the Figure 5.18, the Lorentz force is acting on the flow not only in a horizontal direction but also in a vertical direction. Thus, the flow coming into the region tangential to the wall is deflected slightly away from the wall.

CHAPTER 6

CONCLUDING REMARKSS

A simple mathematical model of MHD flow with plasma discharge was exploited in order to capture the fundamental features of MHD interactions between the electromagnetic field and electrically conducting fluid. In all simulation cases, a uniform and constant electrical conductivity was assumed. This was perhaps a strong assumption for air plasma. However, this assumption allowed us to do a parametric study of the effects of electromagnetic field on the electrically conducting fluid.

Simulation results for channel flow revealed the fundamental MHD related phenomenon, namely, magnetic pressure, and Lorentz force production. Although the magnetic pressure to the conducting fluid was found to be a undesired effect for the application of flow acceleration. However, it was also found that this effect is insignificant unless the strength of magnetic field is very large. This order of magnitude of the magnetic field strength is impractical since the enormous amount of input power will be required.

A role of electric field is to increase the total current, which results in body force acting on the flow. Unlike the current induced by the motion of the fluid and the magnetic field, the current produced by the electric field does not depend on the flow velocity. Thus, in the channel case with uniform electric field and magnetic field, the flow is uniformly affected by them by noting the fact the effect of magnetic pressure is negligible in a relatively low magnitude of magnetic field.

For applications of external flow control, spatially uniform electromagnetic field cannot be achieved as it was mentioned in Chapter5, electrodes and magnets must be located on the same surface. Thus, the effect of MHD on the fluid was always confined into the region of boundary layer.

It should be noted that all the cases tested with the channel were low Reynolds number flows in the range of 5,000~10,000. Flow with low Reynolds number has a low inertial force to viscous force ratio. In this range, the MHD effect on the flow is comparable to the inertial effect. However, the effect of MHD effect on the flow becomes much less compared with the inertial effect in high speed flow. For this reason, it is very difficult to alter the whole flow field using MHD. On the other hand, the potential use of MHD effect is to alter the boundary layer is still promising since the inertial effect in the boundary layer region is still small compared with the viscous effect.

Simulation results for the flow over a cylinder were promising though a high applied voltage and electrical conductivity were required to alter the flow over the cylinder. The significant change in pressure distribution over the surface of the cylinder proved the possible use of MHD technique for aerospace applications. Indeed, Figure 5.30 implies that the resultant force can be obtained by placing pairs of electrodes and magnets only one side of the cylinder. For instance, when the three electrodes used in this simulation were mounted at the bottom portion of the cylinder and substantial voltage was applied, pressure on the bottom portion of the cylinder would increase. As a result, the net force acting in a positive vertical direction can be obtained. In other words, MHD device may serve as a lift generation device for this case.

In conclusion, a MHD simulation based on a primitive mathematical model was able to predict the basic MHD effects. Furthermore, it predicted the significant alternation of the flow over a circular cylinder in terms of pressure distribution. Through these simulations results, fundamental lessons were learned for the design of MHD flow control devices. More sophisticated mathematical model should be examined in order to capture detailed flow phenomenon due to MHD effects.

APPENDIX A

NONDIMENSIONALIZATION OF GOVERNING EQUATIONS

Nondimensionalization of equations

$$x=\frac{\tilde{x}}{\tilde{L}_{ref}}\quad y=\frac{\tilde{y}}{\tilde{L}_{ref}}\quad t=\frac{\tilde{t}}{\tilde{L}_{ref}/\tilde{V}_{ref}}\quad u=\frac{\tilde{u}}{\tilde{V}_{ref}}\quad v=\frac{\tilde{v}}{\tilde{V}_{ref}}$$

$$\mu=\frac{\tilde{\mu}}{\tilde{\mu}_{ref}}\quad \rho=\frac{\tilde{\rho}}{\tilde{\rho}_{ref}}\quad p=\frac{\tilde{p}}{\tilde{\rho}_{ref}\tilde{V}_{ref}^{2}}\quad T=\frac{\tilde{T}}{\tilde{T}_{ref}}\quad e=\frac{\tilde{e}}{\tilde{V}_{ref}^{2}}$$

$$\vec{E}=\frac{\tilde{\vec{E}}}{\tilde{E}_0}\ \sigma=\frac{\sigma}{\sigma_0}\ \vec{B}=\frac{\tilde{\vec{B}}}{B_0}$$

Dimensional governing equations

$$\frac{\partial\tilde{\rho}}{\partial\tilde{t}}+\frac{\partial}{\partial\tilde{x}}\left(\tilde{\rho}\tilde{u}\right)+\frac{\partial}{\partial\tilde{y}}\left(\tilde{\rho}\tilde{v}\right)=0$$

$$\frac{\partial\left(\tilde{\rho}\tilde{u}\right)}{\partial\tilde{t}}+\frac{\partial}{\partial\tilde{x}}\left(\tilde{\rho}\tilde{u}^{2}+\tilde{p}-\tilde{\tau}_{xx}\right)+\frac{\partial}{\partial\tilde{y}}\left(\tilde{\rho}\tilde{u}\tilde{v}-\tilde{\tau}_{yx}\right)=\tilde{J}_y\tilde{B}_z$$

$$\frac{\partial\left(\tilde{\rho}\tilde{v}\right)}{\partial\tilde{t}}+\frac{\partial}{\partial\tilde{x}}\left(\tilde{\rho}\tilde{v}\tilde{u}-\tilde{\tau}_{xy}\right)+\frac{\partial}{\partial\tilde{y}}\left(\tilde{\rho}\tilde{v}^{2}+\tilde{p}-\tilde{\tau}_{yy}\right)=-\tilde{J}_x\tilde{B}_z$$

$$\frac{\partial\tilde{\bar{E}}_t}{\partial\tilde{t}}+\frac{\partial}{\partial\tilde{x}}\left[\tilde{\bar{E}}_t\tilde{u}+\left(-\tilde{K}_t\frac{\partial\tilde{T}}{\partial\tilde{x}}\right)+\tilde{p}\tilde{u}-\tilde{u}\,\tilde{\tau}_{xx}-\tilde{v}\,\overleftrightarrow{\tau}_{xy}\right]$$

$$+\frac{\partial}{\partial\tilde{y}}\left[\tilde{\bar{E}}_t\tilde{v}+\left(-\tilde{K}_t\frac{\partial\tilde{T}}{\partial\tilde{y}}\right)+\tilde{p}\tilde{v}-\tilde{u}\,\tilde{\tau}_{yx}-\tilde{v}\,\tilde{\tau}_{yy}\right]=\tilde{J}_x\tilde{E}_x+\tilde{J}_y\tilde{E}_y$$

Non-diemensional equations

$$\left(\frac{\tilde{\rho}_0\tilde{a}_0}{\tilde{L}_0}\right)\frac{\partial\rho}{\partial t}+\left(\frac{\tilde{\rho}_0\tilde{a}_0}{\tilde{L}_0}\right)\frac{\partial}{\partial x}\left(\rho u\right)+\left(\frac{\tilde{\rho}_0\tilde{a}_0}{\tilde{L}_0}\right)\frac{\partial}{\partial y}\left(\rho v\right)=0$$

For x-momentum equations,

$$\left(\frac{\tilde{\rho}_0\tilde{a}_0{}^2}{\tilde{L}_0}\right)\frac{\partial(\rho u)}{\partial t}+\left(\frac{1}{\tilde{L}_0}\right)\frac{\partial}{\partial x}\left(\tilde{\rho}_0\tilde{a}_0{}^2\rho u^2+\tilde{\rho}_0\tilde{a}_0{}^2p-\frac{\tilde{\mu}_0\tilde{a}_0}{\tilde{L}_0}\tau_{xx}\right)+\left(\frac{1}{\tilde{L}_0}\right)\frac{\partial}{\partial y}\left(\tilde{\rho}_0\tilde{a}_0{}^2\rho uv-\frac{\tilde{\mu}_0\tilde{a}_0}{\tilde{L}_0}\tau_{yx}\right)=\tilde{J}_y\tilde{B}_z$$

$$\left(\frac{\tilde{\rho}_0\tilde{a}_0{}^2}{\tilde{L}_0}\right)\frac{\partial(\rho u)}{\partial t}+\left(\frac{\tilde{\rho}_0\tilde{a}_0{}^2}{\tilde{L}_0}\right)\frac{\partial}{\partial x}\left(\rho u^2+p-\frac{\tilde{\mu}_0}{\tilde{\rho}_0\tilde{a}_0\tilde{L}_0}\tau_{xx}\right)+\left(\frac{\tilde{\rho}_0\tilde{a}_0{}^2}{\tilde{L}_0}\right)\frac{\partial}{\partial y}\left(\rho uv-\frac{\tilde{\mu}_0}{\tilde{\rho}_0\tilde{a}_0\tilde{L}_0}\tau_{yx}\right)=\tilde{J}_y\tilde{B}_z$$

$$\left(\frac{\tilde{\rho}_0\tilde{a}_0{}^2}{\tilde{L}_0}\right)\frac{\partial(\rho u)}{\partial t}+\left(\frac{\tilde{\rho}_0\tilde{a}_0{}^2}{\tilde{L}_0}\right)\frac{\partial}{\partial x}\left(\rho u^2+p-\frac{1}{\mathrm{Re}}\tau_{xx}\right)+\left(\frac{\tilde{\rho}_0\tilde{a}_0{}^2}{\tilde{L}_0}\right)\frac{\partial}{\partial y}\left(\rho uv-\frac{1}{\mathrm{Re}}\tau_{yx}\right)=\tilde{J}_y\tilde{B}_z$$

$$\frac{\partial(\rho u)}{\partial t}+\frac{\partial}{\partial x}\left(\rho u^2+p-\frac{1}{\mathrm{Re}}\tau_{xx}\right)+\frac{\partial}{\partial y}\left(\rho uv-\frac{1}{\mathrm{Re}}\tau_{yx}\right)=\left(\frac{\tilde{L}_0}{\tilde{\rho}_0\tilde{a}_0{}^2}\right)\tilde{J}_y\tilde{B}_z$$

Similar to x-momentum equations,

$$\frac{\partial(\rho v)}{\partial t}+\frac{\partial}{\partial x}\left(\rho uv-\frac{1}{\mathrm{Re}}\tau_{xy}\right)+\frac{\partial}{\partial y}\left(\rho v^2+p-\frac{1}{\mathrm{Re}}\tau_{yy}\right)=-\left(\frac{\tilde{L}_0}{\tilde{\rho}_0\tilde{a}_0{}^2}\right)\tilde{J}_x\tilde{B}_z$$

The right side of x and y-momentum equations can be written as the vector form with the coefficients that come from the process of non-dimensionalizing the lefthand side of equations. Furthermore, using Ohm’s law, current density can be expressed in terms of electric field and magnetic field.

$$\left(\frac{\tilde{L}_0}{\tilde{\rho}_0\tilde{a}_0^{\,2}}\right)\tilde{\vec{J}}\times\tilde{\vec{B}}=\left(\frac{\tilde{L}_0}{\tilde{\rho}_0\tilde{a}_0^{\,2}}\right)\tilde{\sigma}\left(\vec{E}+\tilde{\vec{v}}\times\tilde{\vec{B}}\right)\times\tilde{\vec{B}}$$

$$\left(\frac{\tilde{L}_0}{\tilde{\rho}_0\tilde{a}_0^{\,2}}\right)\tilde{\vec{J}}\times\tilde{\vec{B}}=\left(\frac{\tilde{L}_0}{\tilde{\rho}_0\tilde{a}_0^{\,2}}\right)\tilde{\sigma}\left[E_0\vec{E}+\left(\tilde{a}_0\tilde{B}_0\right)\vec{v}\times\vec{B}\right]\times\left(\tilde{B}_0\vec{B}\right)$$

$$\left(\frac{\tilde{L}_0}{\tilde{\rho}_0\tilde{a}_0^{\,2}}\right)\tilde{\vec{J}}\times\tilde{\vec{B}}=\left[\left(\frac{\tilde{L}_0\tilde{B}_0\tilde{\sigma}E_0}{\tilde{\rho}_0\tilde{a}_0^{\,2}}\right)\vec{E}+\left(\frac{\tilde{L}_0\tilde{B}_0\tilde{\sigma}\tilde{a}_0\tilde{B}_0}{\tilde{\rho}_0\tilde{a}_0^{\,2}}\right)\vec{v}\times\vec{B}\right]\times\vec{B}$$

$$\left(\frac{\tilde{L}_0}{\tilde{\rho}_0\tilde{a}_0^{\,2}}\right)\tilde{\vec{J}}\times\tilde{\vec{B}}=\left[\left(\frac{\tilde{L}_0\tilde{B}_0\tilde{\sigma}E_0}{\tilde{\rho}_0\tilde{a}_0^{\,2}}\right)\vec{E}+\left(\frac{\tilde{L}_0\tilde{B}_0\tilde{\sigma}\tilde{B}_0}{\tilde{\rho}_0\tilde{a}_0}\right)\vec{v}\times\vec{B}\right]\times\vec{B}$$

$$\left(\frac{\tilde{L}_0}{\tilde{\rho}_0\tilde{a}_0^{\,2}}\right)\tilde{\vec{J}}\times\tilde{\vec{B}}=\left[\left(\frac{\tilde{L}_0\tilde{B}_0\tilde{\sigma}E_0}{\tilde{\rho}_0\tilde{a}_0^{\,2}}\right)\vec{E}+\left(\frac{\tilde{L}_0^{\,2}\tilde{B}_0^{\,2}\tilde{\sigma}}{\tilde{\eta}_0}\right)\left(\frac{\tilde{\eta}_0}{\tilde{\rho}_0\tilde{a}_0\tilde{L}_0}\right)\vec{v}\times\vec{B}\right]\times\vec{B}$$

$$\left(\frac{\tilde{L}_0}{\tilde{\rho}_0\tilde{a}_0^{\,2}}\right)\tilde{\vec{J}}\times\tilde{\vec{B}}=\left[\left(\frac{\tilde{L}_0\tilde{B}_0\tilde{\sigma}E_0}{\tilde{\rho}_0\tilde{a}_0^{\,2}}\right)\vec{E}+\left(H_a^{\,2}\right)\left(\frac{1}{\mathrm{Re}}\right)\vec{v}\times\vec{B}\right]\times\vec{B}$$

Let’s look at the first term of the right hand side.

$$\left(\frac{\tilde{L}_0}{\tilde{\rho}_0\tilde{a}_0^{\,2}}\right)\tilde{\vec{J}}\times\tilde{\vec{B}}=\left[\left(\frac{\tilde{L}_0^{\,2}\tilde{B}_0^{\,2}\tilde{\sigma}}{\tilde{\eta}_0}\right)\left(\frac{\tilde{\eta}_0}{\tilde{L}_0\tilde{B}_0}\right)\left(\frac{\tilde{E}_0}{\tilde{\rho}_0\tilde{a}_0^{\,2}}\right)\vec{E}+\left(H_a^{\,2}\right)\left(\frac{1}{\mathrm{Re}}\right)\vec{v}\times\vec{B}\right]\times\vec{B}$$

$$\left(\frac{\tilde{L}_0}{\tilde{\rho}_0\tilde{a}_0^{\,2}}\right)\tilde{\vec{J}}\times\tilde{\vec{B}}=\left[\left(H_a^{\,2}\right)\left(\frac{\tilde{\eta}_0}{\tilde{\rho}_0\tilde{a}_0\tilde{L}_0}\right)\left(\frac{\tilde{E}_0}{\tilde{B}_0\tilde{a}_0}\right)\vec{E}+\left(H_a^{\,2}\right)\left(\frac{1}{\mathrm{Re}}\right)\vec{v}\times\vec{B}\right]\times\vec{B}$$

$$\left(\frac{\tilde{L}_0}{\tilde{\rho}_0\tilde{a}_0^{\,2}}\right)\tilde{\vec{J}}\times\tilde{\vec{B}}=\left[\left(H_a^{\,2}\right)\left(\frac{1}{\mathrm{Re}}\right)\left(\frac{\tilde{E}_0}{\tilde{B}_0\tilde{a}_0}\right)\vec{E}+\left(H_a^{\,2}\right)\left(\frac{1}{\mathrm{Re}}\right)\vec{v}\times\vec{B}\right]\times\vec{B}$$

$$\left(\frac{\tilde{L}_0}{\tilde{\rho}_0\tilde{a}_0^{\,2}}\right)\tilde{\vec{J}}\times\tilde{\vec{B}}=\left[\left(H_a^{\,2}\right)\left(\frac{1}{\mathrm{Re}}\right)(K)\vec{E}+\left(H_a^{\,2}\right)\left(\frac{1}{\mathrm{Re}}\right)\vec{v}\times\vec{B}\right]\times\vec{B}$$

The final non-dimensional form of the right handside of the equation can be written as

$$\left(\frac{\tilde{L}_0}{\tilde{\rho}_0\tilde{a}_0^{\,2}}\right)\tilde{\vec{J}}\times\tilde{\vec{B}}=\left[\left(\frac{H_a^{\,2}K}{\mathrm{Re}}\right)\vec{E}+\left(\frac{H_a^{\,2}}{\mathrm{Re}}\right)\vec{v}\times\vec{B}\right]\times\vec{B}$$

$$\left(\frac{\tilde{L}_0}{\tilde{\rho}_0\tilde{a}_0^{\,2}}\right)\tilde{\vec{J}}\times\tilde{\vec{B}}=\vec{J}\times\vec{B}$$

The non-dimensionalized total current density can be defined as,

$$\vec{J}=\left[\left(\frac{H_a^{\,2}K}{\mathrm{Re}}\right)\vec{E}+\left(\frac{H_a^{\,2}}{\mathrm{Re}}\right)\vec{v}\times\vec{B}\right]$$

$$H_a^{\ 2} = \frac{\widetilde{L}_0^{\ 2} \widetilde{B}_0^{\ 2} \widetilde{\sigma}}{\widetilde{\eta}_0}$$

$$\mathrm{Re} = \frac{\widetilde{\rho}_0 \widetilde{a}_0 \widetilde{L}_0}{\widetilde{\eta}_0}$$

In the vector form, the non-dimensionalized total current density can be written as

$$\vec{J} = \begin{Bmatrix} J_x \\ J_y \end{Bmatrix} = \begin{Bmatrix} \left(\frac{H_a^{\ 2} K}{\mathrm{Re}}\right) E_x + \left(\frac{H_a^{\ 2}}{\mathrm{Re}}\right) v B_z \\ \left(\frac{H_a^{\ 2} K}{\mathrm{Re}}\right) E_y + \left(\frac{H_a^{\ 2}}{\mathrm{Re}}\right)\left(-u B_z\right) \end{Bmatrix}$$

When the magnetic force is derived by taking j from Ohm's law, the Hartmann number will appear. (p38 Sutton&Shermann)

$$H_a^{\ 2} = \frac{\textit{magnetic body force}}{\textit{viscous force}} = \frac{\sigma_0 a_0 B_0^{\ 2}}{\eta_0 a_0 / L_0^{\ 2}} = \frac{\sigma_0 B_0^{\ 2} L_0^{\ 2}}{\eta_0}$$

Non-dimensionalizng the energy equation is performed.

$$\frac{\partial \widetilde{\overline{E}}_t}{\partial \widetilde{t}} + \frac{\partial}{\partial \widetilde{x}}\left[\widetilde{\overline{E}}_t \widetilde{u} + \left(-\widetilde{K}_t \frac{\partial \widetilde{T}}{\partial \widetilde{x}}\right) + \widetilde{p}\widetilde{u} - \widetilde{u}\,\widetilde{\tau}_{xx} - \widetilde{v}\,\overleftrightarrow{\tau}_{xy}\right]$$

$$+ \frac{\partial}{\partial \widetilde{y}}\left[\widetilde{\overline{E}}_t \widetilde{v} + \left(-\widetilde{K}_t \frac{\partial \widetilde{T}}{\partial \widetilde{y}}\right) + \widetilde{p}\widetilde{v} - \widetilde{u}\,\widetilde{\tau}_{yx} - \widetilde{v}\,\widetilde{\tau}_{yy}\right] = \widetilde{J}_x \widetilde{E}_x + \widetilde{J}_y \widetilde{E}_y$$

Let us just look at the right hand side of the energy equation.

$$\left(\frac{\widetilde{L}_0}{\widetilde{\rho}_0 \widetilde{a}_0^{\ 2}}\right)\left(\widetilde{J}_x \widetilde{E}_x + \widetilde{J}_y \widetilde{E}_y\right) = \left(\frac{\widetilde{L}_0}{\widetilde{\rho}_0 \widetilde{a}_0^{\ 2}}\right) \widetilde{\vec{J}} \cdot \widetilde{\vec{E}}$$

$$\left(\frac{\widetilde{L}_0}{\widetilde{\rho}_0 \widetilde{a}_0^{\ 2}}\right) \widetilde{\vec{J}} \cdot \widetilde{\vec{E}} = \left(\frac{\widetilde{L}_0}{\widetilde{\rho}_0 \widetilde{a}_0^{\ 3}}\right) \widetilde{\sigma}\left[E_0 \vec{E} + \left(\widetilde{a}_0 \widetilde{B}_0\right) \vec{v} \times \vec{B}\right] \cdot \left(\widetilde{E}_0 \vec{E}\right)$$

$$\left(\frac{\widetilde{L}_0}{\widetilde{\rho}_0 \widetilde{a}_0^{\ 2}}\right) \widetilde{\vec{J}} \cdot \widetilde{\vec{E}} = \left(\frac{\widetilde{\sigma} \widetilde{E}_0 \widetilde{L}_0}{\widetilde{\rho}_0 \widetilde{a}_0^{\ 3}}\right)\left[E_0 \vec{E} + \left(\widetilde{a}_0 \widetilde{B}_0\right) \vec{v} \times \vec{B}\right] \cdot \vec{E}$$

$$\left(\frac{\widetilde{L}_0}{\widetilde{\rho}_0 \widetilde{a}_0^{\ 2}}\right) \widetilde{\vec{J}} \cdot \widetilde{\vec{E}} = \left[\left(\frac{\widetilde{\sigma} \widetilde{L}_0 E_0^{\ 2}}{\widetilde{\rho}_0 \widetilde{a}_0^{\ 3}}\right) \vec{E} + \left(\frac{\widetilde{\sigma} \widetilde{E}_0 \widetilde{L}_0 \widetilde{B}_0}{\widetilde{\rho}_0 \widetilde{a}_0^{\ 2}}\right) \vec{v} \times \vec{B}\right] \cdot \vec{E}$$

$$\left(\frac{\widetilde{L}_0}{\widetilde{\rho}_0 \widetilde{a}_0^{\ 2}}\right) \widetilde{\vec{J}} \cdot \widetilde{\vec{E}} = \left[\left(\frac{\widetilde{\sigma} \widetilde{L}_0 \widetilde{E}_0 \widetilde{B}_0}{\widetilde{\rho}_0 \widetilde{a}_0^{\ 2}}\right)\left(\frac{\widetilde{E}_0}{\widetilde{a}_0 \widetilde{B}_0}\right) \vec{E} + \left(\frac{\widetilde{\sigma} \widetilde{L}_0 \widetilde{B}_0^{\ 2}}{\widetilde{\rho}_0 \widetilde{a}_0}\right)\left(\frac{\widetilde{E}_0}{\widetilde{a}_0 \widetilde{B}_0}\right) \vec{v} \times \vec{B}\right] \cdot \vec{E}$$

$$\left(\frac{\widetilde{L}_0}{\widetilde{\rho}_0 \widetilde{a}_0^{\ 2}}\right) \widetilde{\vec{J}} \cdot \widetilde{\vec{E}} = K\left[\left(\frac{H_a^{\ 2} K}{\mathrm{Re}}\right) \vec{E} + \left(\frac{H_a^{\ 2}}{\mathrm{Re}}\right) \vec{v} \times \vec{B}\right] \cdot \vec{E}$$

$$\left(\frac{\widetilde{L}_0}{\widetilde{\rho}_0 \widetilde{a}_0^{\ 2}}\right) \widetilde{\vec{J}} \cdot \widetilde{\vec{E}} = K \vec{J} \cdot \vec{E}$$

$$\frac{\partial \widetilde{\overline{E}}_t}{\partial \tilde{t}} + \frac{\partial}{\partial \tilde{x}}\left[\widetilde{\overline{E}}_t \tilde{u} + \left(-\tilde{K}_t \frac{\partial \tilde{T}}{\partial \tilde{x}}\right) + \tilde{p}\tilde{u} - \tilde{u}\,\tilde{\tau}_{xx} - \tilde{v}\,\overleftrightarrow{\tau}_{xy}\right]$$

$$+\frac{\partial}{\partial \tilde{y}}\left[\widetilde{\overline{E}}_t \tilde{v} + \left(-\tilde{K}_t \frac{\partial \tilde{T}}{\partial \tilde{y}}\right) + \tilde{p}\tilde{v} - \tilde{u}\,\tilde{\tau}_{yx} - \tilde{v}\,\tilde{\tau}_{yy}\right] = \tilde{J}_x \tilde{E}_x + \tilde{J}_y \tilde{E}_y$$

Nondimensional equations

$$\frac{\partial \rho}{\partial t} + \frac{\partial}{\partial x}(\rho u) + \frac{\partial}{\partial y}(\rho v) = 0$$

$$\frac{\partial(\rho u)}{\partial t} + \frac{\partial}{\partial x}\left(\rho u^2 + p - \tau_{xx}\right) + \frac{\partial}{\partial y}\left(\rho uv - \tau_{yx}\right) = J_y B_z$$

$$\frac{\partial(\rho v)}{\partial t} + \frac{\partial}{\partial x}\left(\rho vu - \tau_{xy}\right) + \frac{\partial}{\partial y}\left(\rho v^2 + p - \tau_{yy}\right) = -J_x B_z$$

$$\frac{\partial \overline{E}_t}{\partial t} + \frac{\partial}{\partial x}\left[\overline{E}_t u + q_x + pu - u\tau_{xx} - v\tau_{xy}\right]$$

$$+\frac{\partial}{\partial y}\left[\overline{E}_t v + q_y + pv - u\tau_{yx} - v\tau_{yy}\right] = K\left(J_x E_x + J_y E_y\right)$$

$$\tau_{xx} = \frac{2}{3}\frac{\eta}{\mathrm{Re}_L}\left(2\frac{\partial u}{\partial x} - \frac{\partial v}{\partial y}\right) \quad \tau_{xy} = \frac{\eta}{\mathrm{Re}_L}\left(\frac{\partial u}{\partial y} + \frac{\partial v}{\partial x}\right) = \tau_{yx}$$

$$\tau_{yy} = \frac{2}{3}\frac{\eta}{\mathrm{Re}_L}\left(2\frac{\partial v}{\partial y} - \frac{\partial u}{\partial x}\right)$$

$$q_x = -\left(\frac{\tilde{\eta}}{(\gamma-1)\mathrm{Re}_L \Pr}\right)\frac{\partial T}{\partial x} \quad q_y = -\left(\frac{\tilde{\eta}}{(\gamma-1)\mathrm{Re}_L \Pr}\right)\frac{\partial T}{\partial y}$$

$$\vec{J} = \begin{Bmatrix} J_x \\ J_y \end{Bmatrix} = \begin{Bmatrix} \left(\frac{{H_a}^2 K}{\mathrm{Re}}\right)E_x + \left(\frac{{H_a}^2}{\mathrm{Re}}\right)vB_z \\ \left(\frac{{H_a}^2 K}{\mathrm{Re}}\right)E_y + \left(\frac{{H_a}^2}{\mathrm{Re}}\right)\left(-uB_z\right) \end{Bmatrix}$$

$${H_a}^2 = \frac{{\tilde{L}_0}^2 {\tilde{B}_0}^2 \tilde{\sigma}_0}{\tilde{\eta}_0}$$

$$\mathrm{Re} = \frac{\tilde{\rho}_0 \tilde{a}_0 \tilde{L}_0}{\tilde{\eta}_0}$$

$$K = \frac{\tilde{E}_0}{\tilde{B}_0 \tilde{a}_0}$$

APPENDIX B

MAXWELL’S EQUATIONS

$$\nabla \cdot \vec{E} = \frac{\rho_e}{K_0} = \frac{1}{K_0}\sum_s n_s e Z_s$$

$$\nabla \cdot \vec{B} = 0$$

$$\nabla \times \vec{E} = -\frac{\partial \vec{B}}{\partial t}$$

$$\nabla \times \vec{B} = -\mu_0 \left(\vec{J} + K_0 \frac{\partial \vec{E}}{\partial t} + \nabla \times \vec{M}_p \right)$$

Faraday's law of induction

$$\Delta\phi = -\frac{d}{dt}\int_S \vec{B} \cdot d\vec{S}$$

A magnetic field potential "A" is defined

$$\vec{B} = \nabla \times \vec{A}$$

The total electric field consists of two contributions, one is the induced electric field due to the time rate of change of magnetic flux, and another one is externally applied electric field.

$$\begin{aligned} \nabla \times \vec{E} &= \nabla \times \vec{E}' + \nabla \times \vec{E}'' \\ &= -\frac{\partial \vec{B}}{\partial t} + \nabla \times \vec{E}'' \\ &= -\frac{\partial (\nabla \times \vec{A})}{\partial t} + \nabla \times \vec{E}'' \\ &= -\nabla \times \frac{\partial \vec{A}}{\partial t} + \nabla \times \vec{E}'' \end{aligned}$$

Thus,

$$\nabla \times \vec{E} = -\nabla \times \frac{\partial \vec{A}}{\partial t} + \nabla \times \vec{E}''$$

$$\vec{E} = -\frac{\partial \vec{A}}{\partial t} + \vec{E}''$$

$$\vec{E} = -\frac{\partial \vec{A}}{\partial t} - \nabla \phi$$

The above equation is the general expression for the total electric field.
For our applications, we assume the steady state condition. Thus, there is no induced electric field considered.

The electric current in a nonstatic situation can be derived. This can be derived from the conservation of charge similar to the conservation mass.

$$-\int \vec{J}\cdot d\vec{S} = \frac{d}{dt}\int \rho_e dV$$

J: not a total current in this work (total current will be described later)

$$\rho_e = e\sum_s n_s Z_s$$

Using Gauss' theorem, the above equation can be written as

$$-\int \nabla\cdot\vec{J}dV = \frac{d}{dt}\int \rho_e dV$$

$$-\nabla\cdot\vec{J} = \frac{d\rho_e}{dt}$$

$$\vec{J} = \frac{\sum_i eZ_i w_i}{V} = \sum_s n_s eZ_i \vec{v}_s$$

The charge current can be decomposed into a drift current Jd, the effect of helical motion of individual particles, and polarization caused by charge separation.

$$\vec{J} = \vec{J}_d + \nabla\times\vec{M}_\mu + \frac{\partial\vec{P}_e}{\partial t}$$

In addition to the current caused by the motion of charges, changes in the dipole moment appear to be a current, because of the motion of the charges in the dipole.

$$\nabla\cdot\left(\vec{J}_d + \nabla\times\vec{M}_\mu + \frac{\partial\vec{P}_e}{\partial t}\right) = -\frac{d\rho_e}{dt}$$

$$\nabla\cdot\left(\vec{J}_d + \nabla\times\vec{M}_\mu + \frac{\partial\vec{P}_e}{\partial t}\right) + \frac{\partial\left(\nabla\cdot\vec{P}_p\right)}{\partial t} = -\frac{d\rho_e}{dt} + \frac{\partial\left(\nabla\cdot\vec{P}_p\right)}{\partial t}$$

$$\nabla\cdot\left(\vec{J}_d + \nabla\times\vec{M}_\mu + \frac{\partial}{\partial t}\left(\vec{P}_e + \vec{P}_p\right)\right) = -\frac{\partial\left(\rho_e - \nabla\cdot\vec{P}_p\right)}{\partial t} \text{(p21, Sutton \& Sherman)}$$

$$\nabla\cdot\left(\vec{J}_d + \nabla\times\vec{M}_\mu + \frac{\partial\vec{P}}{\partial t}\right) = -\frac{\partial\rho_{et}}{\partial t}$$

Total current

$$\begin{aligned}\vec{J}_t &= \vec{J}_d + \nabla\times\vec{M}_\mu + \frac{\partial\vec{P}}{\partial t}\\ &= \vec{J}_d + \nabla\times\vec{M}_\mu + \frac{\partial\vec{P}_e}{\partial t} + \frac{\partial\vec{P}_p}{\partial t}\\ &= \vec{J} + \frac{\partial\vec{P}_p}{\partial t}\end{aligned}$$

The first three terms represent the current due to the charge motion.

$$\vec{J} = \frac{\sum_i eZ_i w_i}{V} = \sum_s n_s eZ_i \vec{v}_s$$

$$\begin{aligned}\vec{J}_t &= \vec{J} + \frac{\partial \vec{P}_p}{\partial t} \\ &= \sum_s n_s e Z_i \vec{v}_s + \frac{\partial \vec{P}_p}{\partial t}\end{aligned}$$

$$\nabla \times \vec{B} = \mu_0 \vec{J}$$

$$\nabla \times \vec{B} = \mu_0 \vec{J}_d + \mu_0 \nabla \times \vec{M}_\mu \equiv \mu_0 \vec{J}$$

Jd: drift current associated with the motion of the guiding centers of charged particles
The second term: an apparent magnetization current

REFERENCES

[1] Alferov V.I. and Egorov I.V., Hypersonic flow in an MHD-acceleration facility and under full-scale conditions

[2] Sutton, G. and Sherman, A. (1965). Engineering magnetohydrodynamics, Dover Publications, Inc., Mineola, New York

[3] Sutton, G. and Biblarz, O. (2001). Rocket propulsion elements, John Wiley & Sons, Inc.

[4] Lachmann, G. V. (1961). Boundary layer and flow control, Pergamon press, LTD., New York

[5] M. Nishihara, J. W. Rich, W. R. Lempert, I.V. Adamovich, "MHD flow control and power generation in low-temperature supersonic flows", in 37th AIAA Plasmadynamics and Lasers Conference, San Francisco, California, June 2006

[6] J. Menart, J.Shang, C. Atzbach, S. Magoteaux, M. Slagel, and B. Bilheimer, "Total drag and lift measurements in a Mach 5 flow affected by a plasma discharge and a magnetic field", in 43rd AIAA Aerospace Sciences Meeting and Exhibit, Reno, Nevada, January 2005

[7] Rodney Meyer, Munetake Nishihara, Adam Hicks, Naveen Chintala, Michael Cundy, and Walter R. Lempert, "Measurements of Flow Conductivity and Density Flutuations in Supersonic Nonequilibrium Magnetohydrodynamic Flows", AIAA Journal, Vol. 43, No. 9, September 2005

[8] Patel M.P., Ng T.T., and Vasudevan S., "Plasma Actuators for Hingeless Aerodynamic Control of an Unmanned Air Vehicle", in 3rd AIAA Flow Control Conference, San Francisco, California, June 2006

[9] Enloe C.L., McLaughlin. T.E., and Font G.I., "Mechanisms and responses of a single dielectric barrier plasma actuator: Geometric effects", AIAA Journal, Vol. 42, No.3, March 2004

[10] Huang J., Corke T.C., and Thomas F.O., Plasma actuators for separation control of low-pressure turbine blades", AIAA Journal, Vol. 44, No.1, March 2006

[11] Anderson, J.D. (1989). Hypersonic and high temperature gas dynamics, AIAA, Inc., Reston, VA

[12] Gnoffo P.A., Gupta R.N., and Shinn J.L., Conservation equations and physical models for hypersonic air flows in thermal and chemical nonequilibrium, NASA-TP-2867, 1989

[13] Cinnella P. and Grossman B., Upwind techniques for flows with multiple translational temperatures, in 21st AIAA Fluid Dynamics, Plasma Dynamics and Lasers Conference, Seattle, WA, June 1990

[14] Ramshaw J.D. and Change, C.H., Ambipolar diffusion in two-temperature multicomponent plasmas", Plasma Chemistry and Plasma Processing, Vol. 13, No.3, 1993

[15] Fertig M., Dohr A., and Fruhauf H.H., Transport coefficient for high temperature nonequilibrium flows, AIAA, 1998

[16] Canupp P.W., Modeling of neutral gas dynamics in high density plasmas, Ph.D. thesis, Stanford University, June 1997

[17] Ramakanth M., Shashi A., and Vijaya S., Effect of wall conduction in proposed MHD enhanced hypersonic vehicles

[18] Kossyi A., Kostinsky A.Y., Matveyev A.A., and Silakov V.P., Kinetic schme of the non-equilibrium discharge in nitrogen-oxygen mixtures, Plasma Sources Sci. Technol., Vol. 1, No.1, July 1992

[19] Becker K.H., Barker R.J., and Schoenbach K.H., Non-equilibrium air plasmas at atmospheric pressure, Institute of Physics Publishing, 2004

[20] Lieberman M.A., Lichtenberg A.J., Principles of plasma discharges and materials processing, John Wiley & Sons, New York, NY, 1994

[21] Hippler R., Pfau S.M., Schmidt M., Schoenbach K.H., Low temperature plasma physics, John Wiley-VCH, Berlin, 2001

[22] Shang J.S., Gaitonde D.V., and Updike G.A., Modeling magneto-aerodynamic actuator for hypersonic flow control, in 35th AIAA Plasmadynamics and Laser Conference, July 2004

[23] Surzhikov S.T. and Shang J.S., Glow discharge in magnetic field, AIAA 2003-1054, Reno NV, 6-9

[24] Shang J.S., Solving schemes for computational magneto-aerodynamics, Journal of Scientific Computing, Vol. 25, November 2005

[25] Roe P.L., Characteristic-based schemes for the Euler equations, Annual Review of Fluid Mechanics, Vol. 18, January 1986

[26] Toro, E.F. (1999) Riemann solvers and numerical methods for fluid dynamics, Springer, Verlag Berlin Heidelberg, Germany

[27] N. T. Frink, NASA Langley Research Center, "Recent Progress Toward a Three-Dimensional Unstructured Navier-Stokes Flow Solver", 32nd AIAA Aerospace Science Meeting, Reno, Nevada, January 1994.

[28] Hirsch, C. (1990). Numerical computation of internal and external flows, John Wiley & Sons Ltd, Chichester, England

[29] Donea, J. and Huerta, A. (2003). Finite Element Methods for Flow Problems, Wiley
Publishers, Chichester, England.

[30] Alexandrou, A. (2001). Principles of fluid mechanics, Prentice-Hall, Inc., Upper Saddle River, New Jersey

[31] North Atlantic Treaty Organization. (1990). The cases for computation of internal flows in aero engine components, AGARD Advisory Report No.275

BIOGRAPHICAL INFORMATION

Takahiro Sonoda was born in Kanagwa, Japan, in 1982. He received his elementary and middle school education in Hadano, and completed his high school education at Atsugi high school. He came to U.S. to join the University of Texas at Arlington in 2001, and graduated in 2005 with a Bachelor of Science in Aerospace Engineering. He chose to remain in UTA to pursue a Masters degree in Aerospace Engineering. His areas of research during graduate study include development of discontinuous Galerkin finite element method and magnetohydrodynamics.